ANNUAL REVIEWS

Annual Review of Physical Chemistry

Quantum State–Resolved Structure and Dynamics of C₆₀ Fullerenes

Lee R. Liu^{1,2,3} and Jun Ye^{1,2}

¹JILA, National Institute of Standards and Technology and University of Colorado, Boulder, Colorado, USA

²Department of Physics, University of Colorado, Boulder, Colorado, USA

³Current affiliation: Department of Chemistry, Purdue University, West Lafayette, Indiana, USA; email: leeliu@purdue.edu

ANNUAL CONNECT

www.annualreviews.org

- · Download figures
- Navigate cited references
- · Keyword search
- Explore related articles
- Share via email or social media

Annu. Rev. Phys. Chem. 2025. 76:303-28

First published as a Review in Advance on February 4, 2025

The Annual Review of Physical Chemistry is online at physchem.annualreviews.org

https://doi.org/10.1146/annurev-physchem-082423-013137

Copyright © 2025 by the author(s). This work is licensed under a Creative Commons Attribution 4.0 International License, which permits unrestricted use, distribution, and reproduction in any medium, provided the original author and source are credited. See credit lines of images or other third-party material in this article for license information.



Keywords

C₆₀ fullerenes, cryogenic buffer gas cooling, cold molecules, high-resolution infrared spectroscopy, cavity-enhanced direct absorption spectroscopy, frequency comb spectroscopy

Abstract

The C_{60} fullerene molecule has been the subject of intense study for four decades, starting with its identification in the mass spectra of carbon soot in 1985. In this review, we focus on the achievement of ultra-high-resolution spectroscopy of gas phase neutral C_{60} , heralded by the observation of quantum state–resolved infrared spectra in 2019. C_{60} is now the largest and most symmetric molecule for which rovibrational quantum state resolution has been achieved, motivating the use of large molecules for studying complex quantum systems with symmetries and degrees of freedom not readily available in other composite systems. We discuss the theory, challenges, and experimental techniques of high-resolution C_{60} spectroscopy and recent experimental results probing the structure, dynamics, and interactions of C_{60} enabled by quantum state resolution.

1. INTRODUCTION

Large molecules straddle the boundary of atoms and extended materials (1). Like atoms, molecules are finite objects with a discrete spectrum of collective excitations that can be resolved spectroscopically. Like materials, molecules comprise many atoms bonded at short distances of \sim 1 Å. The short bond lengths entail strong intramolecular interactions leading to collective excitations (i.e., vibrations) at relatively high energies (tens of terahertz).

The distinctive feature of molecules is that these energy scales are high enough to be frozen out even at relatively high temperatures while also being low enough that the associated radiative lifetimes are reasonably long, around a second. In addition, the unique combination of free rotations, discrete rotational symmetries, mesoscopic size, and extensive rotation-vibration coupling makes large molecules a new frontier for realizing emergent behavior not realizable in any other composite quantum system accessible to tabletop experiments. Understanding, and eventually controlling, these unique properties relies on infrared spectroscopy coupled with modern advances in cooling, spectral resolution, and absorption sensitivity.

1.1. Infrared Spectroscopy

Infrared spectroscopy is a powerful technique to identify chemical compounds with high specificity, even when spectra from many different molecules are overlapping in frequency (2). It therefore finds numerous applications (see, e.g., 2, 3): detecting explosives (4), analyzing human breath for medical diagnostics (5–7), environmental (8, 9) and industrial process (10) monitoring, and understanding the chemical composition of outer space (11–15). Furthermore, because of the intimate relation between molecular structure and the fundamental forces and particles, infrared spectroscopy can also determine the value of fundamental constants (16) or test the symmetrization postulate (17–19). Despite these diverse applications, the perspective of this review is to understand how quantum state–resolved infrared spectroscopy not only detects and identifies molecules but also learns about their properties at an unprecedented level of detail.

The simplest form of spectroscopy is direct absorption spectroscopy. A coherent light source illuminates a sample of molecules and the laser's frequency is scanned while its transmission through the sample is monitored. At specific laser frequencies, the light resonantly excites oscillating molecular dipoles and is absorbed (20, 21). The laser frequencies corresponding to absorption dips constitute the molecular spectrum. If the oscillating dipoles originate from vibrations of the molecule, the spectrum lies primarily in the infrared region (22).

Dipole selection rules allow vibrations and rotations to be driven simultaneously, so a sufficiently well-resolved infrared spectrum will also contain the rotational spectrum of the molecule (23). Infrared spectra encode molecular structure: Vibrational frequencies arise from the stiffness and arrangement of molecular bonds, while rotational frequencies arise from the moment of inertia about the molecule's principal axes (24). Indeed, the sensitivity of infrared spectroscopy to structural differences between molecules is exquisite: Vibrational isotope shifts due to the addition of a single neutron to one of the carbon atoms in C_{60} can be on the order of 1 cm⁻¹ (25), easily resolvable in the gas phase. Quantum state–resolved infrared spectra can also inform rotational energy surfaces (RES), the effective Hamiltonian that governs rotational dynamics in the frame of the molecule (26). Finally, spectral line shifts and broadening probe the molecule's interactions with its environment, including those due to collisions (27–29), solvent interactions [e.g., in liquid He droplets (30–33)], or electromagnetic fields (34–37). Thus, quantum state–resolved infrared spectroscopy allows us to probe structure, dynamics, and even interactions of molecules.

For small, volatile molecules, these techniques are well-established. However, achieving a similar level of insight into large molecules requires high absorption sensitivity and overcoming large

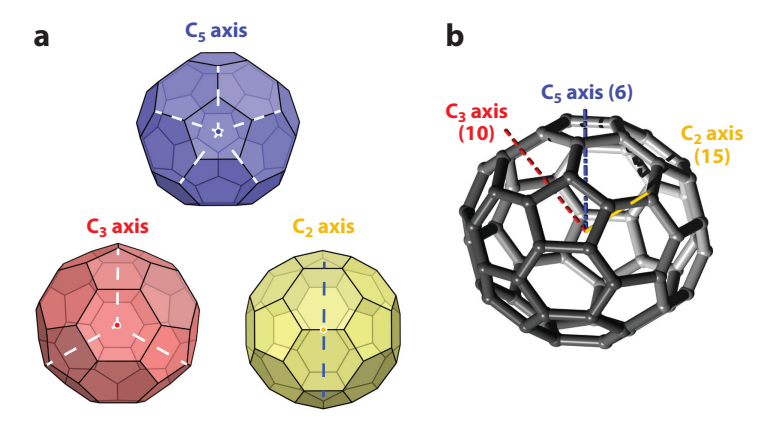


Figure 1

Rotational symmetries of $^{12}C_{60}$. (a) Views of a truncated icosahedron along the three different types of rotational symmetry axes. C_i is an i-fold rotational symmetry axis. (b) Ball-and-stick model of C_{60} , with three different types of rotational symmetry axes labeled to show their relative orientations. The number of times each symmetry-equivalent axis occurs is listed in parentheses. Figure adapted from Reference 42 with permission from AAAS.

internal partition functions and density of states. Therefore, innovative experimental techniques, including cryogenic buffer gas cooling, optical frequency comb spectroscopy, and cavity-based sensitivity enhancement, are required.

1.2. ¹²C₆₀

This review focuses on infrared spectroscopy of the molecule $^{12}C_{60}$, the largest and most symmetric molecule for which quantum state–resolved infrared spectra have been observed (38). C_{60} is a spherical top molecule, meaning its moments of inertia about three orthogonal axes are equal. It belongs to the icosahedral (I_b) point group, described in numerous references (see, e.g., 39–41). Its rotational symmetry elements are depicted in **Figure 1**. I_b additionally contains the inversions, reflections, and improper rotations of the icosahedron and has an order of 120. It is rare in that (a) it is not a crystallographic point group due to its fivefold axis of rotation and (b) no other point group contains I_b as a subgroup. Few molecules in nature exhibit this exceptionally high symmetry.

In 1985, Kroto, Smalley, Curl, and coworkers (43) reported the spontaneous formation of a 60-carbon molecule in laser vaporized graphite. Based on satisfying the valences of 60 carbon atoms, it was hypothesized to take on a closed spheroidal shape, the now famous truncated icosahedron. This eliminates dangling bonds but requires unstable pentagonal defects in the hexagonal carbon lattice (44–47). C₆₀ happens to be the smallest molecule in which pentagons are separated by at least one hexagon, minimizing the curvature (48). This results in the molecule's characteristic shape, discrete rotational symmetry axes, and remarkable stability.

Infrared vibrational spectra were measured for thin films of C_{60} (49–51) and found to match closely to theoretical predictions for the vibrational normal mode frequencies of C_{60} (52). In particular, despite a total of 46 distinct normal modes, only four distinct dipole-active modes were visible in infrared spectra, consistent with predictions of group theory (53).

Resolving individual rotational states of $^{12}C_{60}$ was only achieved 30 years later in our laboratory, by employing infrared frequency comb spectroscopy, cavity enhanced absorption detection, and buffer gas cooling to overcome the enormous vibrational density of states and vibrational partition functions at the $^{12}C_{60}$ sublimation temperature (38). Quantum state resolution opens the gate to

observing ¹²C₆₀'s unique level structure, rotation-vibration dynamics, and interactions with other atoms and molecules.

2. INTRINSIC LIMITS TO QUANTUM STATE RESOLUTION

Spectral lines can be broadened by pressure, typically on the order of 10 MHz/Torr, and temperature, about 10 MHz for the 8.4- μ m infrared band of C₆₀ at 100 K. Additionally, transitions originating from thermally occupied excited vibrational states contribute red-shifted hot bands (54) that congest the infrared spectrum. These forms of broadening and congestion obscure energy level structure and suppress peak absorption cross sections, but they can be managed by reducing sample pressure and temperature and increasing absorption sensitivity.

However, there remains an intrinsic limit to achieving high spectral resolution, particularly in large, excited molecules: intramolecular vibrational energy redistribution (IVR) (55). The density of vibrational states $\rho_{\rm vib}$ has approximately a power-law scaling with vibrational energy content (56). At sufficiently high $\rho_{\rm vib}$, zero-order vibrational states are mixed by anharmonicity (55). The vibrational state prepared by laser excitation no longer overlaps completely with the true eigenstates of the molecule, and the subsequent time evolution leads to lifetime broadening that washes out spectral structure. It has been observed that IVR occurs with a sharp onset when $\rho_{\rm vib}$ reaches a value of around 10 to ~100 states/cm⁻¹ (57–59).

The striking effect of IVR on spectra of increasingly complex molecules is shown in Figure 2a,b (59, 60). Both adamantane ($C_{10}H_{16}$) and diamantane ($C_{14}H_{20}$) are similar in size and belong to the diamondoid family of molecules possessing rigid carbon cage frameworks. Yet the rotational structure of diamantane is completely washed out, whereas that of adamantane is well-resolved in the 3,000 cm⁻¹ C-H stretch region. In addition to the fact that the vibrational density of states increases exponentially with atom number, diamantane has many low-frequency vibrational modes that contribute to rapid growth in the vibrational density of states with vibrational energy content (Figure 2c). Symmetry also plays an important role in mitigating IVR by diluting the effective local density of vibrational states. In the high energy limit, the ratio of the symmetry selected to total vibrational density of states approaches p^2/g , where p is the dimension of the symmetry species being selected for and g is the order of the molecular point group (61, 62). The high symmetry of adamantane restricts anharmonic coupling, and therefore IVR, due to symmetry selection rules (63-67). Symmetry selection motivates a shift toward large molecules with even higher symmetry such as ¹²C₆₀. Furthermore, in general, avoiding IVR in increasingly large molecules also inevitably entails probing at lower energies, in the mid- to far-infrared region.

3. EXPERIMENTAL METHODS

The ¹²C₆₀ isotopolog does not exhibit a pure rotational spectrum due to a lack of a permanent dipole moment. Additionally, due to its inversion symmetry, even centrifugal distortion cannot induce a dipole moment as in methane (40, 70). The dipole moment must be induced by electronic or vibrational degrees of freedom. At electronic energies, the higher Doppler broadening and density of states may render the quantum state resolution of such a large molecule impossible. We therefore turn to infrared vibrational spectroscopy.

Several properties of C_{60} make it amenable to high-resolution infrared spectroscopy. First, the rigidity of C_{60} sets the lowest vibrational energy spacing at a relatively high energy, 270 cm⁻¹ (69). This suppresses the vibrational density of states and ensures that vibrations can be frozen out around 150 K, accessible with liquid nitrogen cooling. Second, C_{60} possesses a dipole-active vibrational mode labeled $T_{1u}(3)$ with a fundamental transition wavelength of 8.4 μ m, corresponding

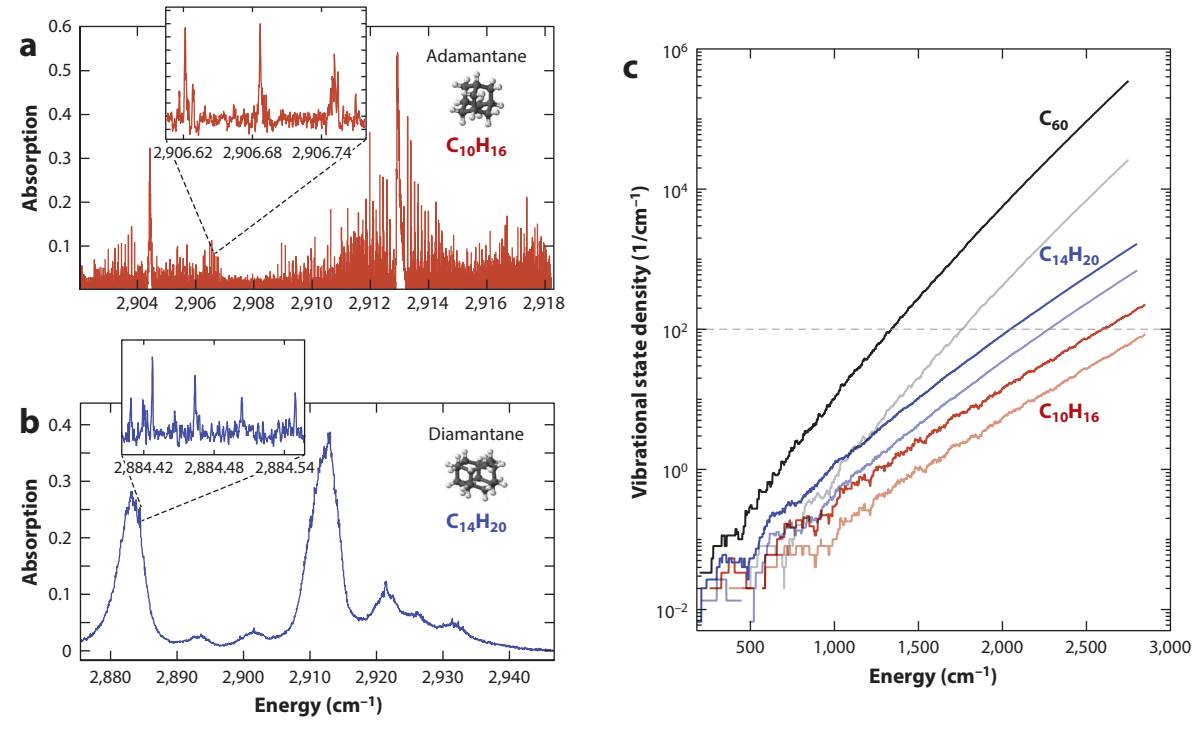


Figure 2

Size limits and intramolecular vibrational energy redistribution (IVR). (a) A portion of the C–H stretching spectral manifold of adamantane. The inset shows the resolved rotational structure. (b) The absorption spectrum of diamantane in the C–H stretching region. The spectrum is essentially continuous, with no well-resolved rotational structure. The inset shows the rare appearance of narrow features above the continuous background (the inset spectrum has been high-pass filtered for visual clarity). The width of these features is consistent with the expected Doppler broadened linewidth, and the spacing between them matches the expected rotational line spacing. (c) The vibrational density of states for several large hydrocarbons. In increasing order, the vibrational density of states versus vibrational energy is shown for adamantane ($C_{10}H_{16}$), diamantane ($C_{14}H_{20}$), and $^{12}C_{60}$. These curves were calculated by applying a direct state count algorithm to calculated (68) and observed (69) vibrational frequencies. The dark lines are the total density of states and the lighter lines are the dipole active symmetry-selected density of states. The symmetry selection is more severe in $^{12}C_{60}$. The horizontal line at 100 states per cm $^{-1}$ marks the empirical threshold symmetry selected state density for IVR (55, 58). Panels a and b adapted with permission from Reference 60.

to an energy of 1,185 cm⁻¹. The local vibrational density of states near the upper state is below the 100 states/cm⁻¹ IVR threshold (**Figure 2**c), and lasers at 8.4 μ m are commercially available and do not overlap a strong water absorption line.

We can estimate the magnitude of the $^{12}C_{60}$ absorption signal at 8.4 μm at 300 K and 1 Torr. The Beer-Lambert law states that the intensity transmitted through an absorbing medium is

$$I(\omega) = I_0 \exp(-\alpha(\omega)z)$$
 1.

$$\approx I_0(1-\alpha(\omega)z),$$
 2.

$$\alpha(\omega) = \Delta \rho_{C_{60}} \sigma_0 g(\omega), \qquad 3.$$

where I_0 is the incident intensity, $\alpha(\omega)$ is the absorption coefficient, z is the sample optical path length, $\Delta \rho_{C_{60}}$ is the difference in $^{12}\mathrm{C}_{60}$ number density in the ground versus upper state, σ_0 is

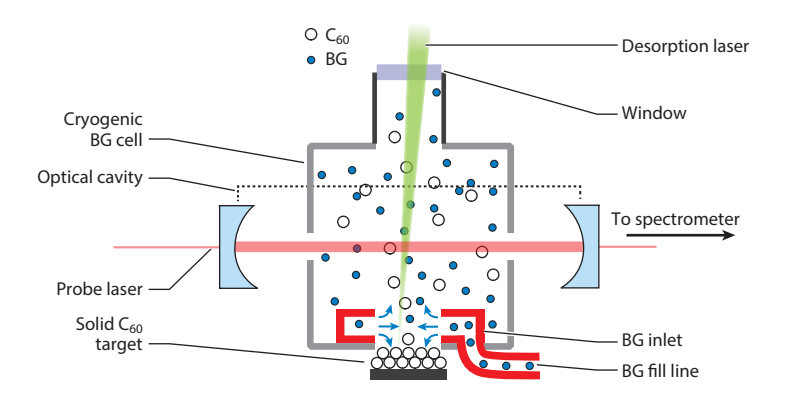


Figure 3

Apparatus for quantum state—resolved infrared spectroscopy of $^{12}C_{60}$. $^{12}C_{60}$ vapor is produced by laser desorption from a thin film target (alternately, sublimation from an oven). Buffer gas (BG), precooled to around 80 K, flows over the target face through an inlet. C_{60} molecules collide with BG and diffuse throughout the cryogenic BG cell where they are probed by an infrared laser. The cell is surrounded by a high-finesse cavity to enhance the effective interaction length and intracavity optical power. The light transmitted through the cavity is incident on a spectrometer.

the frequency integrated absorption cross section, and $g(\omega)$ is the area-normalized absorption lineshape.

The integrated vibrational absorption cross section is 9.4 km/mol (71). The pressure- and thermally broadened linewidth is approximately $10\,\mathrm{MHz}$ (72). The most highly occupied rotation-vibration state contains approximately 3×10^{-8} of the total population. In the presence of high-order tensor perturbations, the peak absorption cross section will be suppressed further by about a factor of ten (42). Finally, to provide the requisite cooling and prevent clustering of large molecules, the molecules of interest are mixed at a relative concentration of a few parts per million into an inert buffer gas to allow for sufficient vibrational relaxation (73–75) (Section 3.1). Altogether this gives a peak absorbance of one to ten parts per billion per meter of interaction length in the quantum state–resolved limit. State-resolved infrared spectroscopy of large molecules in the gas phase therefore requires a long interaction length, low density, sensitive detection, and sufficient cooling to suppress internal partition functions (76). We discuss how this feat is achieved in practice through cryogenic cooling; long-wavelength, frequency-stabilized laser sources; and optical cavity enhancement (**Figure 3**).

3.1. Cold C₆₀ Vapor Source

Cold molecular vapor can be produced by volatilizing a species of interest into a cryogenically cooled cell filled with inert buffer gas such as helium, neon, or argon (75, 77). The buffer gas serves two purposes: (a) Diffusion through the buffer gas prolongs the time that the molecules spend in the gas phase, enhancing the probing time, and (b) collisions with the buffer gas cool the molecules' internal and translational degrees of freedom, with higher pressure yielding more frequent collisions and more efficient cooling. Thus, high-resolution spectroscopy can be achieved in the buffer gas cell directly, provided the buffer gas pressure is high enough to facilitate cooling while also being sufficiently low to mitigate pressure broadening (59) and the formation of van der Waals clusters (78).

Due to the mismatch in timescales between a collision and a vibrational period (75, 79), however, vibrational cooling is generally challenging. This is particularly true for large molecules due

to their low vapor pressure and large vibrational partition functions. C_{60} sublimates at 1,000 K, at which point each molecule contains 7.4 eV of vibrational energy. Quantum state–resolved spectroscopy of $^{12}C_{60}$ therefore requires maximizing the total number of collisions while minimizing heat transfer from the molecular vapor source to the cryogenic buffer gas cell.

Two vapor sources played a key role in observing $^{12}C_{60}$ infrared spectra. The oven source is a bored-out copper cylinder containing C_{60} powder heated to 1,000 K (38). It is positioned a few millimeters from an aperture in the buffer gas cell. The aperture is surrounded by an annular inlet that flows approximately 75 standard cubic centimeters per minute of buffer gas over the face of the aperture, entraining C_{60} into the cell. The thermal mass of the oven ensures uniform C_{60} yield but at the price of a 1-kW heat load. At a buffer gas pressure of \sim 0.3 Torr, C_{60} undergoes \sim 106 buffer gas collisions in the tens of milliseconds it takes to diffuse to the probing region (72), which is sufficient for vibrational cooling of C_{60} (38). However, managing the conductive and radiative heat transfer from the oven to the buffer gas cell requires the high cooling capacity afforded by evaporating liquid nitrogen at a rate of several liters per hour. This limits the buffer gas temperature to be above 77 K and around 150 K in practice. The buffer gas species is also chosen to be Ar, which is ten times less thermally conductive than He while also possessing sufficient vapor pressure at 150 K. The use of Ar instead of He has been observed to exacerbate $^{12}C_{60}$ –buffer gas cluster formation, which depletes the spectroscopic signal from bare $^{12}C_{60}$ and adds spectral congestion.

The oven can be substituted with a laser-desorbed C_{60} vapor source consisting of a thin-film C_{60} target deposited on a metal substrate (depicted in **Figure 3**). A green continuous-wave (CW) laser with a peak power of 2 W is focused onto the target to locally heat and desorb C_{60} molecules (80). In pulsed operation, the time-averaged optical input power is less than 1 W. In addition, laser-desorbed C_{60} molecules are rapidly adsorbed by the cryogenic chamber walls, allowing the C_{60} concentration to be controlled by the desorption laser with a 10- to \sim 100-ms response time. This enables the rapid subtraction of laser intensity fluctuations during data collection. The reduced heat load is compatible with a He cryostat and permits the use of He buffer gas to reach lower temperatures and mitigate clustering. The disadvantages are the lower C_{60} density and transient behavior of hot versus cold C_{60} , which is still not completely characterized. Nevertheless, <10% variation in C_{60} shot-to-shot yield was demonstrated, dominated by variations in the thickness of the deposited C_{60} film (80).

3.2. Optical Detection

One way to increase sensitivity is through optical cavity enhancement (see, e.g., 81 and 82 for a comprehensive review). The cavity consists of two low-loss, high-reflectivity mirrors facing each other. Light enters through one partially transmitting mirror and bounces back and forth inside the cavity multiple times before leaking out, enhancing the effective optical path length and intracavity power. The enhancement factors are proportional to $\mathcal F$ and $\mathcal F^2$, respectively, where $\mathcal F=\frac{2\pi}{\mathcal L}$ is the cavity finesse and $\mathcal L$ is the total loss of the cavity including the transmission and absorption of the mirrors.

The laser source can be either a frequency comb or single-frequency CW laser. Whereas CW laser spectroscopy offers high sensitivity in a narrow frequency band, frequency comb spectroscopy provides simultaneous detection capability over its entire broadband spectral coverage, mitigating potential systematic drifts and uncertainties in frequency scans. One powerful strategy is to obtain survey spectra with the comb to map out interesting spectral regions, then zoom into interesting narrow frequency regions with the CW laser.

A frequency comb is a laser whose frequency spectrum consists of stable, regularly spaced teeth, or modes, forming a ruler in frequency space typically spanning \sim 10 THz. The frequency

of the *i*th comb mode is defined by the relation $f_i = f_0 + i \times f_{\text{rep}}$; hence, spectroscopy using direct frequency comb absorption simultaneously offers large bandwidth and high-frequency resolution, limited by the comb linewidth of approximately 10 kHz. The molecular absorption of each comb mode can be read out simultaneously using a comb mode–resolving spectrometer (59, 83).

Since the comb mode structure matches the transmission spectrum of an optical enhancement cavity, it is possible to efficiently couple many comb modes into an optical cavity to combine broadband coverage and high-frequency resolution of the comb with the high sensitivity afforded by the cavity.

To improve the absorption sensitivity in a narrow frequency range, one can use a CW laser. A popular CW source is the quantum cascade laser (QCL) (84); however, the typical 1-MHz freerunning linewidth of the QCL is still too wide to be efficiently coupled into a high-finesse cavity with a linewidth of approximately 20 kHz. One solution is to implement additional optical feedback with an external reference cavity (85–90). Coupling the QCL output into the apex mirror of a three-mirror V-shaped reference cavity ensures that off-resonant light is reflected specularly off-axis, while light resonant with the cavity returns back along the input beam to provide optical feedback to the laser. The stabilized QCL output is thus narrowed to <10 kHz. One of the mirrors of the reference cavity is mounted on a piezo to stretch the cavity length and, with it, the QCL frequency. During a frequency scan, the length of the reference cavity is monitored interferometrically with a stable reference laser and converted to a relative frequency excursion. The stabilized QCL light can also be sent into a spectrometer prior to the frequency scan to calibrate the absolute frequency.

4. STRUCTURE: ZERO-ORDER SPECTROSCOPIC CONSTANTS, PERTURBATIONS, AND BOSONIC EXCHANGE STATISTICS

 $^{12}C_{60}$ is simultaneously the isotopolog with the highest natural abundance, no hyperfine structure, and highest degree of symmetry. The high symmetry decimates the effective vibrational (Section 2) and rotational (Section 4.2) density of states, simplifying the level structure and reducing congestion. Therefore, $^{12}C_{60}$ is expected to yield the strongest and most well-resolved spectroscopic signal among all C_{60} isotopologs. Below we discuss the first observation of resolved rotational lines of the $^{12}C_{60}$ isotopolog in infrared spectra, enabled by efficient vibrational cooling, cavity enhancement, and probing in the mid-infrared region. The measured linewidths are ~ 10 MHz wide and consistent with Doppler and pressure broadening, showing no evidence of additional broadening due to IVR. Resolved rotational lines can be assigned quantum numbers to extract spectroscopic constants related to the rotational constant, Coriolis constant, and vibrational energy. Crucially, this allows us to establish the zero-order rotational progressions from which higher-order intramolecular perturbations can be deduced. Rotational line intensities probe individual rotational state populations, yielding the rotational temperature. Finally, we observe the modulation of rotational line intensities due to icosahedral nuclear spin weights.

4.1. First Light: Resolving Individual Rotational Lines

The rotationally resolved infrared spectrum of $^{12}C_{60}$ was first observed in a liquid nitrogen cooled buffer gas cell, along with an oven source, frequency comb probe, and an enhancement cavity with $\mathcal{F}=6,000$ providing a minimum absorption sensitivity of $\alpha_{\min}=2.2\times10^{-7}~\mathrm{cm}^{-1}\mathrm{Hz}^{-1/2}$ per comb mode (38). At \sim 0.3-Torr Ar buffer gas pressure, a narrow and well-resolved absorption feature emerged at 8.4 μ m, corresponding to the $T_{1u}(3)$ fundamental band (**Figure 4a**). In particular, the Q-branch appears as three sharp but unresolved profiles (**Figure 4b**) while the R-branch exhibits

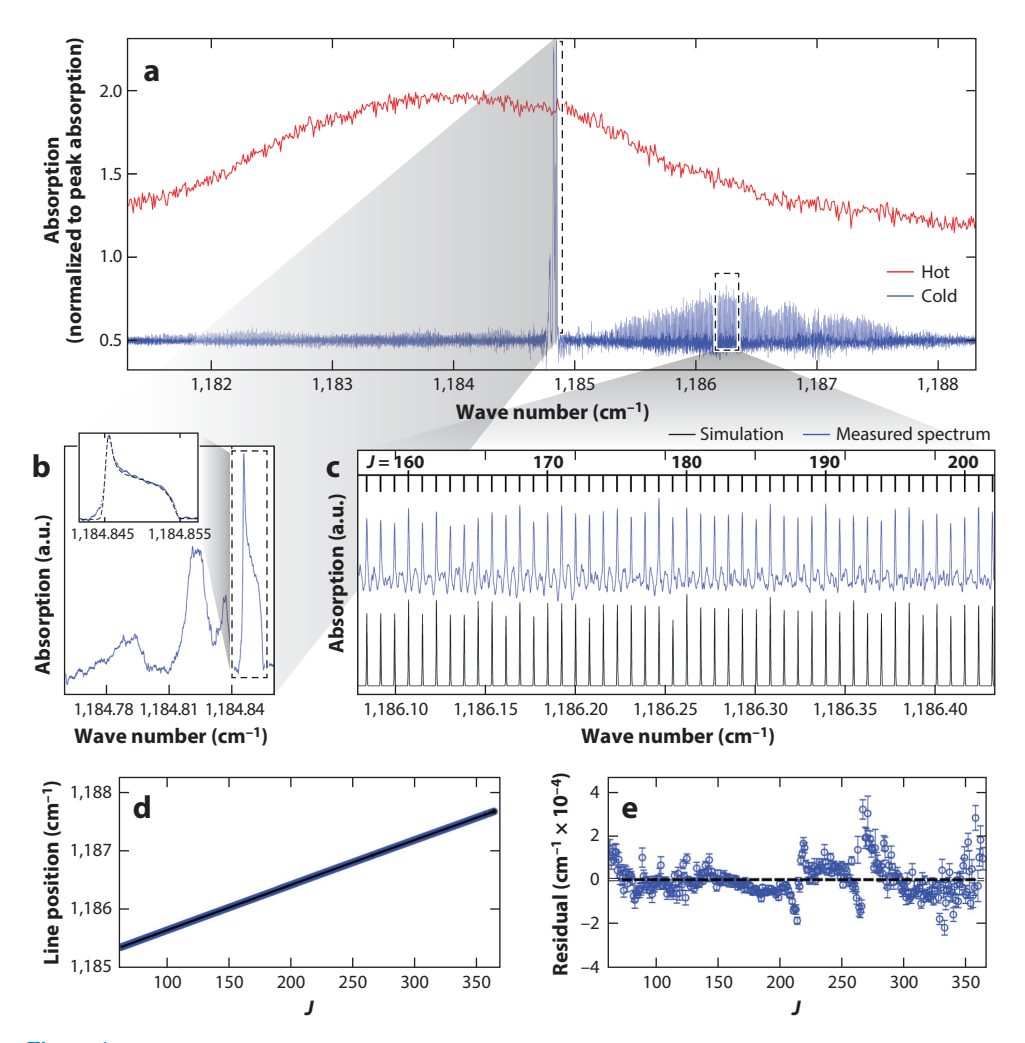


Figure 4

Spectroscopic patterns of the infrared active vibrational band of $^{12}C_{60}$ near 8.4 µm. (a) Measured spectra of cold and hot C_{60} . The measured hot spectrum shows broad, unresolved absorption owing to many thermally occupied vibrational states. The cold spectrum exhibits sharp, well-resolved rotational structure from transitions out of the ground vibrational state [normalized to peak absorption (norm.)]. (b) The Q-branch region of the spectrum contains several features. The highest wave number feature is assigned as the Q-branch of the $^{12}C_{60}$ isotopolog. In the inset, the dashed line represents a fit to a simple quartic centrifugal distortion contour. The additional features at lower frequencies may be due to spectral fractionation or the singly substituted $^{13}C^{12}C_{59}$ isotopolog. (c) The R-branch shows agreement between the expected intensity patterns from the simulation (black trace) and the measured spectrum (blue trace). The tie line above the spectrum indicates the lower-state J value of each observed R(J) transition. (d) The R(J) line positions plotted versus lower-state J display a very linear trend from J=60 to 360. (e) The residuals from the fit of Equation 13 to these line positions exhibit apparent avoided crossings near J=215 and 275, which are possible signatures of local dark-state perturbers in the upper state. The error bars are 1σ line-center uncertainties determined from lineshape fit residuals. Figure adapted from Reference 38 with permission from AAAS.

a resolved rotational progression extending over approximately 300 lines. Below, we present the zero-order expressions for these transition frequencies.

To account for vibration-rotation coupling, it is convenient to invoke the concept of vibrational angular momentum. The vibrational angular momentum vector ℓ describes a deformation of the molecule's equilibrium geometry that circulates around the molecule without involving any tumbling of the molecular frame. The tumbling, or pure rotational angular momentum, is therefore $\mathbf{R} = J - \ell$, where \mathbf{J} is the total angular momentum vector.

In the vibrational ground state, $\ell = 0$ and R = J, so the energy is given by

$$E_0 = B''J(J+1),$$
 4.

which is identical to the energy of a rigid linear rotor with rotational constant B'' (24).

In the first excited vibrational state, we have $\ell=1$. In spherical tops, the infrared active vibrational modes (i.e., those with dipole symmetry) are triply degenerate. The first vibrational excited state therefore sorts into three Coriolis manifolds corresponding to ℓ parallel, perpendicular, or antiparallel to J. After subtracting the vibrational zero-point energy, their energies are

$$E_1^+ = \hbar\omega + B'J(J+1) + 2B'\zeta^2 + 2B'\zeta J$$
 $R = J+1,$ 5.

$$E_1^0 = \hbar\omega + B'J(J+1) + 2B'\zeta^2 - 2B'\zeta$$
 $R = J,$ 6.

$$E_1^- = \hbar\omega + B'J(J+1) + 2B'\zeta^2 - 2B'\zeta(J+1) \qquad R = J-1,$$
 7.

where ω is the vibrational angular frequency; ζ is the Coriolis constant, which ranges from -1 to 1 and is determined by the particular geometry of the vibrational mode; and B' is the rotational constant in the vibrational excited state. E_1^+, E_1^0 , and E_1^- split linearly from each other as J increases due to Coriolis coupling between ℓ and J. These three Coriolis manifolds are labeled $T_{1u}^{(+)}, T_{1u}^{(0)}$, and $T_{1u}^{(-)}$, respectively, where T_{1u} labels the irreducible representation in I_b with dipole symmetry. In the absence of perturbations and applied fields, the spherical top rotational states have a (2J+1)(2R+1) degeneracy, arising from the lab-frame and molecule-frame degeneracies, respectively.

In the linear dipole approximation, the selection rules for fundamental transitions in spherical tops are (91)

$$\Delta R = \Delta k_R = 0, 8.$$

$$\Delta J = 0, \pm 1, \qquad 9.$$

$$\Delta m = 0, \pm 1, \tag{10}$$

where k_R is the projection of **R** along a molecule-fixed axis and m is the projection of **J** along a lab-fixed axis. Subtracting Equation 4 from Equations 5–7 yields the P-, Q-, and R-type transitions corresponding to $\Delta J = -1$, 0, and +1. In spherical tops, the P-, Q-, and R-branches access mutually exclusive Coriolis manifolds, with transition frequencies given by

$$v^+ = \Delta + \Delta B J (J+1) + 2B' \zeta J$$
 P-branch, 11.

$$v^0 = \Delta + \Delta B J (J+1) - 2B' \zeta$$
 O-branch, 12.

$$\nu^{-} = \Delta + \Delta B J (J+1) - 2B' \zeta (J+1)$$
 R-branch, 13.

where $\Delta = \hbar\omega + 2B'\zeta^2$ and $\Delta B = B' - B''$. Energy level diagrams and allowed fundamental transitions for the first few *J* levels, including the effect of nuclear spin statistics (Section 4.2), are shown in **Supplemental Figure 1**.

Supplemental Material >

Equation 13 can be rewritten as $v^- = a + bJ + cJ^2$ and the spectroscopic constants a, b, and c are obtained from a fit to the measured line positions (**Figure 4d**,e). In units of cm⁻¹, we find

$$a = v_0 + (2\bar{B} + \Delta B)(1 - 2\zeta)$$
 = 1,184.86196(3), 14.

$$b = 2\bar{B}(1-\zeta) + \Delta B(2-\zeta)$$
 = 0.0078300(3), 15.

$$c = \Delta B$$
 = $-2.876(6) \times 10^{-7}$. 16.

Here, $\bar{B} = (B + B')/2$ and $\Delta B = B' - B$. These values are consistent with the calculated ζ constant (92) and a radius of \sim 3.6 Å inferred from gas phase electron diffraction (93).

The integrated absorption of each J spectral feature can be fitted to a rotational Boltzmann distribution, yielding a rotational temperature of about 150 K. Together with the absence of hot bands, this indicates that C_{60} has likely been cooled to near its vibrational ground state (38).

4.2. Signature of Icosahedral Symmetry in Nuclear Spin Statistics

Accounting for the bosonic exchange statistics of 12 C atoms further suppresses the 2R+1 zero-order molecule-fixed frame degeneracy factor mentioned in Section 4.1. In particular, since each 12 C atom in 12 C₆₀ is a spinless, indistinguishable boson, the nuclear wave function is of A_g symmetry in I_b . In the electronic and vibrational ground state, the rotational wave function must be of A_g or A_u symmetry. For R < 30, only states of R = 0, 6, 10, 12, 15, 16, 18, 20–22, and 24–28 satisfy this requirement and the remaining R values are forbidden. For $R \ge 30$, all rotational quantum numbers are associated with at least one state, and the relative contrast in rotational line intensities due to nuclear spin statistics diminishes with increasing R (40). In the high-R limit, the rotational degeneracy of 12 C₆₀ approaches (2J+1)(2R+1)/60. At 150 K, the presence of icosahedral nuclear spin weights can be seen in the modulation of rotational line intensities, although the relative contrast is low (**Figure 4**c).

Lowering the temperature concentrates more of the population into states of low R, where the full contrast modulation of rotational line intensities can be observed. By probing with a QCL coupled into a cavity with increased finesse ($\mathcal{F}=12,500$), the absorption sensitivity was increased by approximately a thousandfold. Furthermore, employing a laser desorption source to reduce the rotational temperature to 100 K increased the absorption signal for R < 30 by a factor of 2. These experimental improvements allowed for the direct confirmation of icosahedral nuclear spin weights (80) (**Figure 5**). Similar to the sparse vibrational spectra mentioned in Section 1.2, the decimation of rotational states is a stark confirmation of $^{12}C_{60}$'s remarkable icosahedral symmetry.

4.3. Conclusion

Although the infrared spectroscopy of spherical tops cannot obtain ground state rotational splittings via combination differences (94) due to restrictive selection rules (Equations 11–13), perhaps the most important result to emerge from quantum state resolution of the $T_{1u}(3)$ band of $^{12}C_{60}$ is the zero-order rotational progression, from which it becomes possible to identify higher-order perturbations. These include (a) the existence of avoided crossings in the R-branch, based on the residual of their peak positions from the fit to a linear rotational progression (**Figure 4**a,e); (b) fractionation of the Q-branch into three unresolved features (**Figure 4**b); and (c) strong and extensive fractionation in the P-branch spectrum (**Figure 4**a). The reason for strong

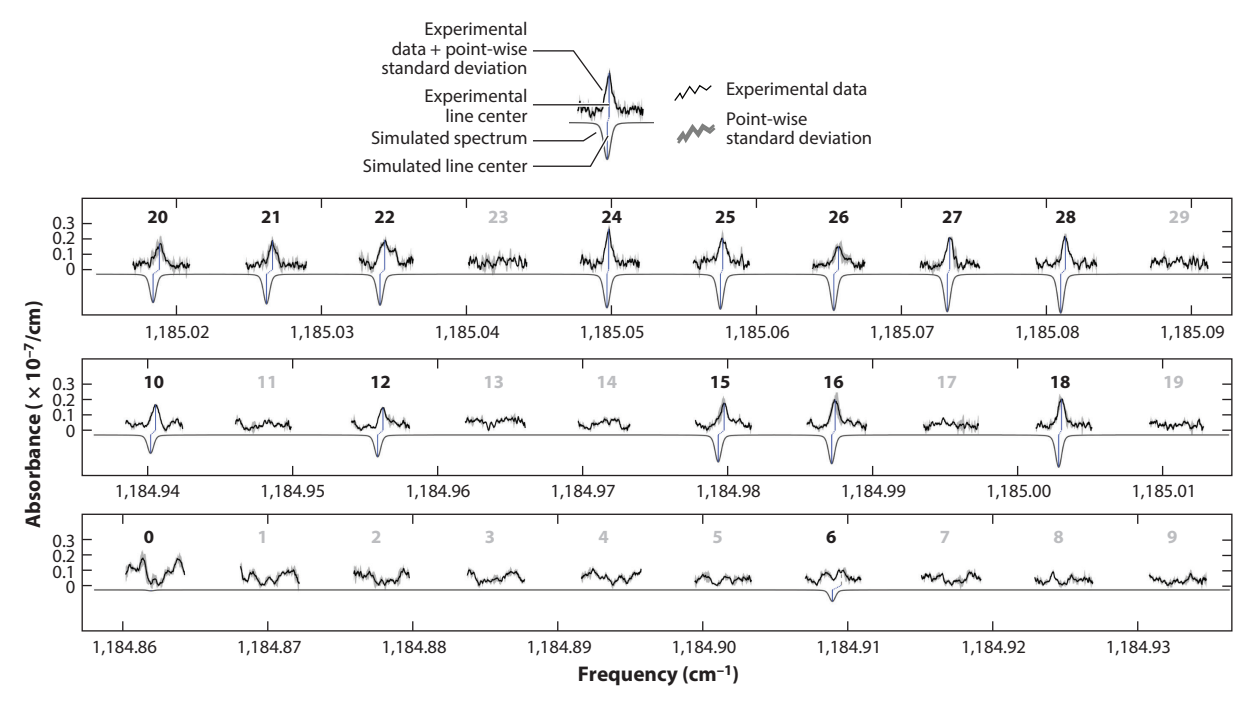


Figure 5

Full contrast icosahedral nuclear spin statistics of $^{12}C_{60}$. The complete absorption spectrum of the $T_{1u}(3)$ R-branch in the range of J=0-29 is shown. Experimental data (black) are the average of 200–400 raw spectra, with the light gray error bands representing the point-wise standard deviation. The simulated spectrum (gray, inverted) was derived from spectroscopic constants determined in Reference 38, assuming a rotational temperature of 100 K and including nuclear spin weights. Notably, the complete absence of many R(J) transitions, as predicted by bosonic exchange statistics and the molecule's icosahedral symmetry, is clearly visible. There is an increasing $\sim 5-15$ -MHz blue shift of experimental line centers (gray vertical lines) from the simulated spectrum as J decreases from 29 to 0, continuing the trend seen in Reference 38. Note, we tentatively assign R(J=6) to the higher-frequency peak in the doublets (dashed vertical line). Additional features at J=6 and 22 and at very low J are deemed to be real. Figure adapted from Reference 80.

perturbations to the P-branch but not the R-branch remains an open question. At the current level of resolution and rotational temperature, the perturbations that give rise to the Q-branch fractionation also remain a mystery. Spectroscopy on the remaining dipole-active bands at 7.0, 17.4, and 19.0 μ m and better rotational cooling to concentrate the population into lower R states can help answer these questions and elucidate the structure of $^{12}C_{60}$ beyond the zero-order approximations of Section 4.1.

5. DYNAMICS: ERGODICITY BREAKING INDUCED BY ROTATIONS

The physical properties of a finite system depend on its shape (95, 96). Rotating a finite system can effect shape changes due to the noninertial forces in the rotating frame. While there are generally technical obstacles to rotating cold atom ensembles or materials at sufficiently high angular momentum to significantly affect dynamics, gas phase molecules routinely exhibit free rotations with significant coupling to other molecular degrees of freedom. Examples of rotation-induced intramolecular dynamics, observed in rotationally resolved infrared spectra of ¹²C₆₀, are rotational ergodicity breaking and restoring as the molecule rotates faster and faster.

Ergodicity, the central tenet of statistical mechanics, requires an isolated system to explore all available phase space constrained by energy and symmetry. Mechanisms for violating ergodicity

are of interest for probing nonequilibrium matter and protecting quantum coherence in complex systems. While the phenomenon of IVR has been understood in terms of the ergodicity breaking of vibrational energy transport in molecules, here, the ergodicity of the molecule's rotation is considered.

Molecular rotation is a convenient degree of freedom from a technological standpoint due to the radio frequency or microwave energy scales and long intrinsic coherence times. Furthermore, as mentioned in Section 4.1, the quantum numbers associated with pure rotation involve projections along molecule-fixed axes, which can, in the presence of high-order perturbations, be spectroscopically resolved and manipulated without orienting the molecule in the lab frame.

5.1. Rotational Fine Structure

Probing the 8.4-µm vibrational band with a QCL and a cavity with a finesse of 12,500, we achieve a minimum absorption sensitivity $\alpha_{\rm min} = 2.1 \times 10^{-10} \, {\rm cm^{-1} Hz^{-1/2}}$ per spectral element, sufficient to detect the individual perturbed rotational lines in the P-branch of **Figure 4a**. After subtracting the rigid rotor contributions to the transition frequency (Section 4.1), only the *R*-dependent rotational fine structure patterns remain (**Figure 6a**). With no applied fields, the molecular Hamiltonian respects spherical and inversion symmetry, so its terms can be classified according to irreducible representations of the rotation-inversion group with the additional requirement that they transform like the totally symmetric irreducible representation in the molecular point group (97). In

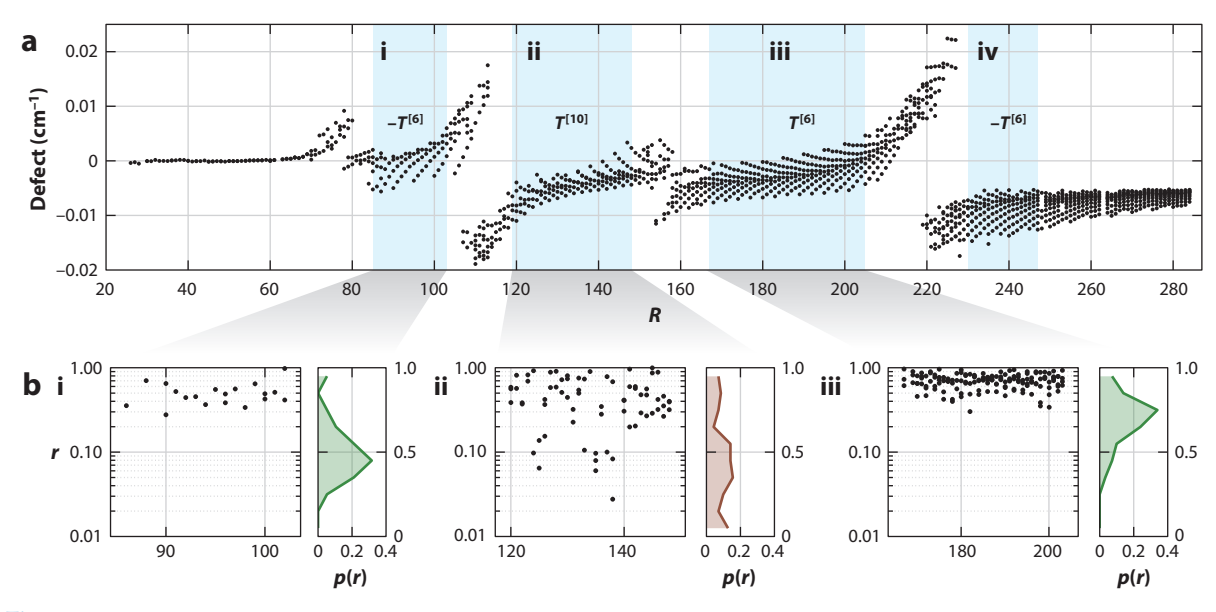


Figure 6

Breaking and restoring rotational ergodicity in $^{12}C_{60}$. (a) Tensor defect plot of $T_{1u}^+(3)$, after subtracting off the scalar contribution to the P-branch transition frequencies (Equation 11). Four avoided crossings with varying strengths are seen at $R \approx 80$, 110, 160, and 220. Defect patterns resemble eigenvalue spectra of icosahedral invariant tensor operators. The dominant icosahedral tensor character $\pm T^{[k]}$ is labeled for each of the sections i-iv. (b) Energy-level statistics in ergodic and nonergodic regimes. Left panels show the gap ratio r as a function of R calculated from sections i-iii of the defect spectrum in panel a. Gap ratios are only plotted at R values for which the peak counts match the calculated rotational degeneracy. Right panels show the normalized distribution p(r) of gap ratios aggregated over sections i-iii. Note the change from logarithmic to linear r scale between the left and right panels. Sections i and iii exhibit level repulsion, a signature of ergodicity, whereas section i does not, indicating ergodicity breaking. Figure adapted from Reference 42 with permission from AAAS.

Section 4.1 we only discussed the zero-order scalar terms in the molecular Hamiltonian, which trivially fulfill these criteria. They do not, however, account for any possible perturbations that would lift the 2R + 1 molecule-frame rotational degeneracy and give rise to a rotational fine structure. For $^{12}C_{60}$, such tensor perturbations are constructed by projecting the spherical tensor operators onto A_g in I_b (98, 99). The two lowest-order terms are given by

$$T^{[6]} = \frac{\sqrt{11}}{5} T_0^{(6)} + \frac{\sqrt{7}}{5} (T_5^{(6)} + T_{-5}^{(6)}),$$
 17.

$$T^{[10]} = \frac{\sqrt{3 \cdot 13 \cdot 19}}{75} T_0^{(10)} - \frac{\sqrt{11 \cdot 19}}{25} (T_5^{(10)} - T_{-5}^{(10)}) + \frac{\sqrt{3 \cdot 11 \cdot 17}}{75} (T_{10}^{(10)} + T_{-10}^{(10)}),$$
 18.

where $T_q^{(k)}$ is the *q*th component of a spherical tensor operator of rank *k*. The eigenvalue spectra are shown in **Figure 7a**, and the corresponding RES (discussed in Section 5.3) are shown in **Figure 7b**. These eigenvalue spectra, or tensor defects, constitute the possible corrections to the zero-order energies of Equations 5–7. It is no coincidence that the rank *k* of the terms appearing in the ${}^{12}C_{60}$ Hamiltonian match the allowed rotational angular momenta in the vibrational and electronic ground state: $R = 0, 6, 10, \cdots$ mentioned in Section 4.2.

To a good approximation, at sufficiently low angular momenta, R alone determines the eigenvalue spectra of the operators in Equations 17 and 18 due to the Wigner-Eckart theorem. Only the overall R-dependent scaling can depend on J, ℓ , and the dynamical origin of the perturbations (97). Note, however, that since the rotational spectra of $^{12}C_{60}$ at 150 K span hundreds of R's, this approximation may not be valid throughout the entire range of observed rotational states.

Despite lacking a priori knowledge of the dynamical origin of the P-branch perturbations, the highly restricted form of the operators in Equations 17 and 18 enables the assignment of portions of the spectrum in **Figure 6a** to sixth- or tenth-rank tensor perturbations. Indeed, the rotational fine structure patterns are identical to the calculated eigenvalue spectra of **Figure 7a** up to an overall sign, R-dependent offset, and scaling. The avoided crossings evident in **Figure 6a** suggest that the rotational fine structure arises from the intramolecular coupling of the $T_{1u}^{(+)}(3)$ state to zero-order dark vibrational states that become accidentally degenerate at specific R values.

5.2. Quantum Ergodicity of Molecular Rotations

Quantum ergodicity is associated with eigenstates extended in phase space that can be strongly coupled by local perturbations, inducing energy-level repulsion. By contrast, ergodicity breaking is associated with the existence of localized eigenstates that are not strongly coupled by perturbations. Their energies are uncorrelated and do not exhibit level repulsion (100–102). Ergodic and nonergodic dynamics are therefore respectively associated with level repulsion and its absence (100). A useful diagnostic tool is the distribution p(r), where r is the ratio of consecutive level spacings, or energy gap ratio e_i (103, 104):

$$r_i = \min\left(\frac{s_i}{s_{i-1}}, \frac{s_{i-1}}{s_i}\right),\tag{19}$$

$$s_i = e_{i+1} - e_i.$$
 20.

In the limit of $r \to 0$, level repulsion in an ergodic system causes $p(r) \to 0$, and for a nonergodic system $p(r) \to \text{constant}$.

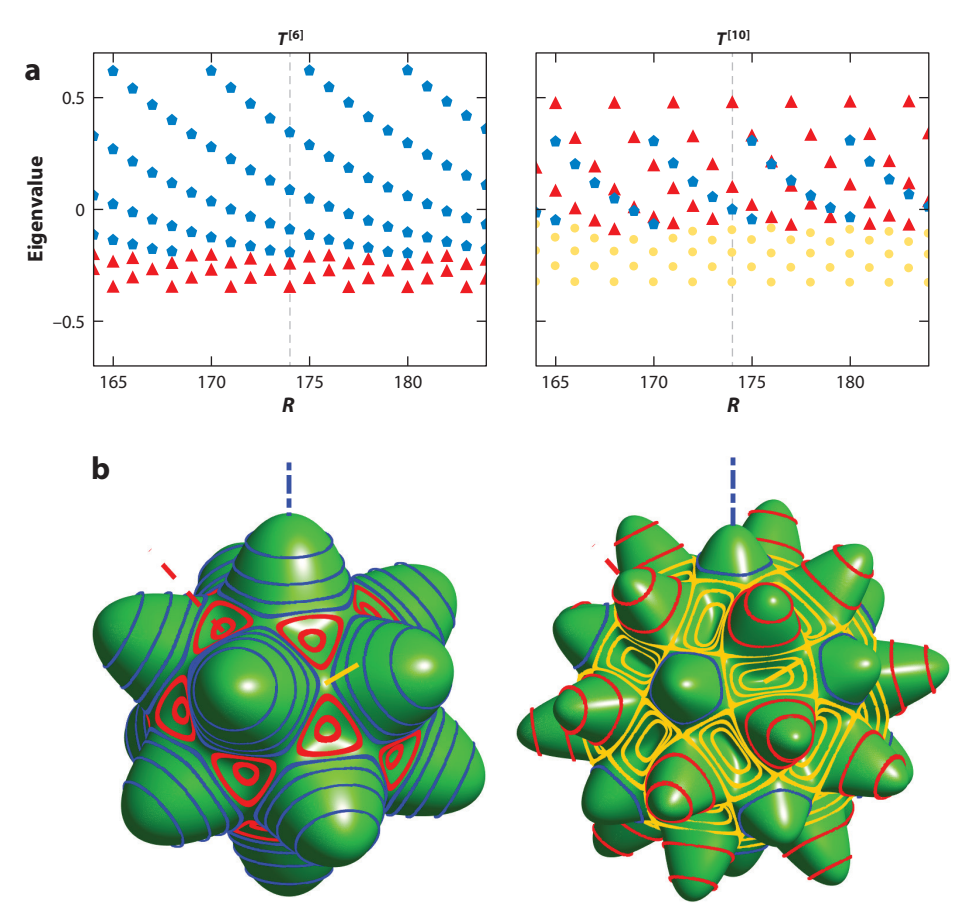


Figure 7

Eigenvalue spectra of icosahedral invariant tensors and rotational energy surfaces. (a) Eigenvalue spectra of Equation 17 for $T^{[6]}$ (left) and Equation 18 for $T^{[10]}$ (right). (b) Rotational energy surfaces for $T^{[6]}$ (left) and $T^{[10]}$ (right), constructed by replacing the $T_q^{(k)}$ in Equations 17 and 18 with spherical harmonics $Y_{kq}(\theta,\phi)$. A spherical offset has been added for clarity. Level curves corresponding to eigenvalues at R=174 in panel a are shown. For $^{12}C_{60}$, the rotational eigenstates consist of symmetric superpositions of all symmetry- and energy-equivalent orbits. The color labeling of symmetry axes and orbits is the same as in **Figure 1**. Figure adapted from Reference 42 with permission from AAAS.

At the Doppler and pressure-broadening-limited frequency resolution of ~10 MHz, and far away from the avoided crossings (where peak assignment is complicated by intensity stealing), all 2R + 1 molecule-frame rotational angular momentum components are accounted for in the measured P-branch spectrum. This is facilitated by the severe symmetry selection of $^{12}C_{60}$ rotational states (Section 4.2). Furthermore, since the R-branch shows little to no rotational fine structure (38), we assume the 2R + 1 degeneracy of the shared ground state is preserved so that the rotational fine structure observed in the P-branch originates from perturbations of the upper state only. This contrasts favorably with $T_{1u}^{(+)}(3)$ zero-order molecular constants, which cannot be determined straightforwardly in infrared spectroscopy due to restrictive spherical top selection rules (94) (Section 4.1). We can therefore analyze the energy gap ratios of the tensor defect spectrum directly in order to characterize the absence or presence of level repulsion in the $T_{1u}^{(+)}(3)$ state rotational multiplets (103–106) (**Figure 6b**).

The energy gap ratios in sections i and iii of **Figure 6**, corresponding to $R = 80{\text -}110$ and 156–220, respectively, exhibit level repulsion, while those in section ii, corresponding to $R = 110{\text -}156$, exhibit no level repulsion. Therefore, when ${}^{12}\text{C}_{60}$ is excited to the $T_{1u}^{(+)}(3)$ vibrational state, it breaks, then restores, ergodicity as it rotates faster and faster.

5.3. Intuition: The Rotational Energy Surface

To understand the physical origin of ergodicity breaking and restoring, it is instructive to plot the tensor perturbations in terms of the corresponding RES, which takes the form of icosahedral harmonics (26, 107–110) (**Figure 7b**). Icosahedral harmonics are constructed by replacing the $T_q^{(k)}$ in Equations 17 and 18 with spherical harmonics $Y_{kq}(\theta, \phi)$, where θ and ϕ are the polar and azimuthal angles in the molecule frame (111–113). RES possess the same C_5 , C_3 , and C_2 rotational symmetry axes as $^{12}C_{60}$.

After adiabatically eliminating molecular vibrations, the effective dynamics in the frame of the molecule are described in a similar manner to the rotational ellipsoid for rigid tops (114): $\bf R$ describes isoenergetic orbits precessing about the symmetry axes of a RES (26, 115). The altitude of the RES along (θ, ϕ) represents the energy cost of orienting $\bf R$ along (θ, ϕ) in the frame of the molecule. The difference between the rotational ellipsoid and the RES is that the latter can also account for deformations of the molecule as a function of the molecule-frame orientation of $\bf R$ due to centrifugal distortion. Hence, the RES of a spherical top molecule can be nonspherical if the centrifugal distortion is anisotropic. Quantum mechanically, only discrete level curves whose altitudes correspond to the eigenvalues of $T^{[6]}$ or $T^{[10]}$ in a fully symmetrized fixed-R subspace are permitted. These orbits trace out the closed contours on the RES in Figure 7b. The orbits may also be obtained directly from the RES: They are the symmetrized superpositions of symmetry-equivalent classical orbits that satisfy a Bohr quantization condition (26, 99).

Figure 7 shows that for $T^{[6]}$ all level curves lie at a different altitude, preserving ergodicity. For $T^{[10]}$, the C_5 -type orbits and C_3 -type orbits lie on symmetry distinct hills and can become accidentally degenerate while separated by a large tunneling barrier. The quantum tunneling between these two types of orbits is unable to restore the ergodicity: The tunneling integral between C_5 and C_3 is exponentially small in R (116), whereas the level spacing only scales as 1/R. Consequently, the tunneling barriers break ergodicity between the hexagonal and pentagonal orbits. This is reflected in the lack of level repulsion between their respective sets of eigenvalues.

5.4. Conclusion

This review highlights several features of $^{12}C_{60}$ unimolecular dynamics: (a) High-resolution spectra can probe dynamics (specifically, the transport of angular momentum) in the molecule frame without requiring orientation or trapping. (b) Provided high sensitivity and quantum state resolution are maintained, a broad thermal ensemble is actually an advantage; the thermal ensemble samples molecules at many angular momenta, providing a comprehensive map of the effective rovibrational Hamiltonian for R ranging from 30 to \sim 300. In particular, the changing patterns of rotational fine structure as a function of R reveal what would happen if one could rotate the molecule faster and faster, even though no such control over the molecules is actually exerted in the experiment. (c) The ergodicity is broken as a function of molecular rotation, not temperature; ergodicity is broken and restored again as this control parameter increases; and ergodicity breaking occurs without symmetry breaking. This phenomenon is expected to be general to molecules of sufficiently high symmetry, highlighting the importance of searching for novel emergent behavior in large, symmetric molecules.

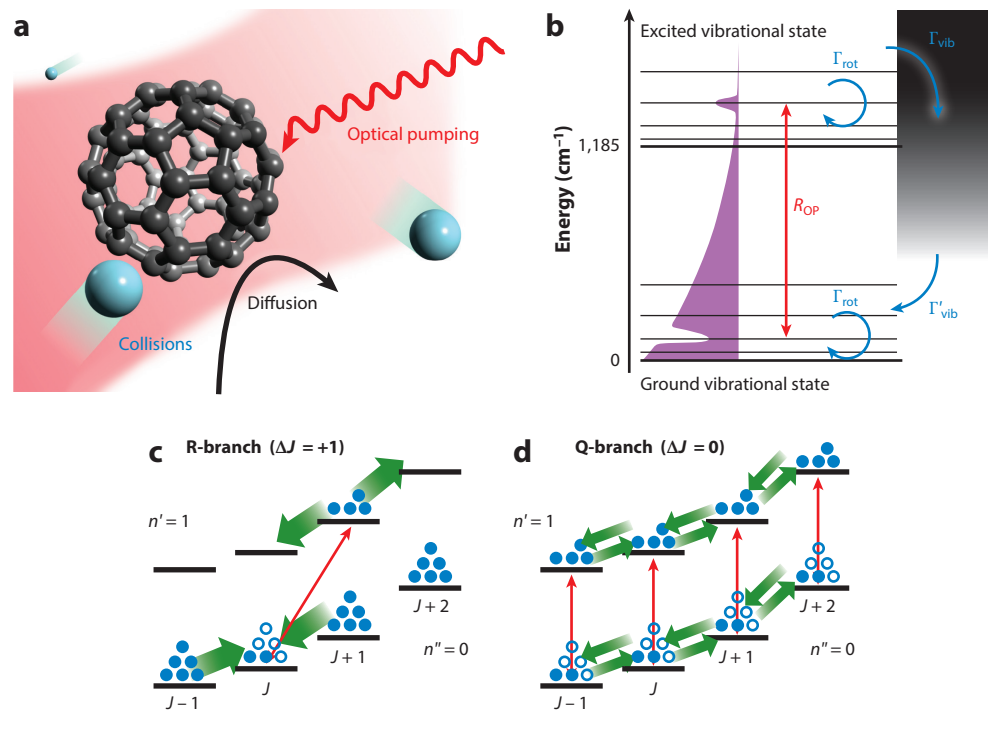


Figure 8

Collisional quenching of $^{12}C_{60}$. (a) Depiction of various physical processes probed by the C_{60} infrared absorption measurement. (b) Energy-level diagram of $^{12}C_{60}$ undergoing collisional relaxation. Optical pumping at a rate R_{OP} drives the 8.4- μ m $T_{1n}(3)$ vibrational band of $^{12}C_{60}$. Collisions with the buffer gas redistribute the rotational population at a rate of Γ_{rot} , assumed to be identical in n''=0 and n'=1. Vibrational relaxation is modeled in two steps: loss of the vibrational population from n'=1 into the dense reservoir of dark vibrational states at a rate of Γ_{vib} , and leakage from the dense reservoir into n''=0 at a rate of Γ'_{vib} . The filled purple curve depicts the steady-state population distribution. (c) State-selective pumping in the R-branch. Only a single transition can be resonantly pumped at a time; therefore, rotational relaxation from C_{60} -buffer gas collisions efficiently redistributes pumped rotational populations (green arrows). (d) Multistate pumping in the Q-branch, with many transitions (up to \sim 75 at the band head) being pumped simultaneously. Intuitively, saturation of the Q-branch is largely sensitive to rotational relaxation, while saturated absorption spectra therefore disentangles the rotational and vibrational inelastic contributions to the total relaxation rate. Figure adapted with permission from Reference 72.

6. INTERACTIONS: COLLISIONAL QUENCHING

Having studied the structure and dynamics of an isolated $^{12}C_{60}$ molecule, we now turn to the interactions of $^{12}C_{60}$ degrees of freedom with the environment, specifically the quenching of rotations and vibrations due to collisions between $^{12}C_{60}$ and the buffer gas (**Figure 8***a*). Interactions can be encoded not only on the positions of absorption lines but also on their lineshape profiles and the response of internal state populations to an external drive. The high sensitivity afforded by the QCL probe and enhancement cavity allows kinetics to be extracted from lineshapes. Moreover, the high intracavity intensity allows for optically pumping internal state populations out of thermal equilibrium.

These results inform collisional cooling schemes and provide the first step toward understanding how to protect the quantum coherence of internal degrees of freedom of $^{12}C_{60}$. In particular,

its high degree of rotational symmetry and stiff cage structure might be expected to hinder rotational and vibrational quenching, respectively, while the higher rotational and vibrational density of states due to its large size may facilitate quenching.

6.1. Collision Broadening and Cross Sections

Two physical mechanisms contribute to the collision broadening of an absorption line: (a) Fourier broadening due to finite state lifetimes and (b) pure dephasing (117–119). The finite lifetime of rotation-vibration states is primarily due to inelastic collisions with the buffer gas that change the state of the molecule. Radiative decay and IVR are insignificant at the experimentally relevant excitation energies and timescales. Dephasing arises when the $^{12}C_{60}$ -buffer gas complex samples a range of intermolecular distances during a collision. Due to the difference in the ground and upper state intermolecular potentials (120), the collision leads to a loss of phase coherence between the molecular transition dipole and a driving optical field. The dephasing interaction is typically strongest at short range (120, 121) and can be referred to as an elastic collision since it involves the exchange of linear or angular momentum between the collision partners but not energy (122, 123).

The probability that a particular collisional interaction takes place between two particles is quantified by their collision cross section σ and may depend on the relative speed and quantum numbers of the two collision partners. The mean collision rate in a thermal ensemble is approximately $\Gamma = \rho_N \langle \sigma \rangle \langle v_{\rm rel} \rangle$, where ρ_N is the buffer gas number density and $\langle \sigma \rangle$ and $\langle v_{\rm rel} \rangle$ are the thermal averages of the total collision cross section and relative speed between the two collision partners, respectively. For elastic collisions, the error incurred from using $\langle \sigma \rangle \langle v_{\rm rel} \rangle$ instead of $\langle \sigma v_{\rm rel} \rangle$ is about 2% over the experimentally relevant temperature range. This collision rate furnishes the absorption lines with a pressure-broadened linewidth $\gamma = 2\Gamma/2\pi$, where the factor of 2 is due to the fact that both the ground and upper states experience collisions (122, 124).

Elastic and vibrationally and rotationally inelastic collisions contribute to the total (pressure-broadened) linewidth γ_{PB} . Disentangling these processes, described in the next section, yields quantitative information about the intermolecular interaction potentials between $^{12}C_{60}$ and various buffer gas species.

6.2. Saturation of Q- and R-Branches: Disentangling Rotational and Vibrational Relaxation

Sections 4 and 5 discussed experiments done in the unsaturated or linear absorption regime. This occurs at low intensity, specifically when the rate of photon absorption per molecule is much slower than the rate of inelastic collisions that tend to restore thermal equilibrium. Therefore, $\Delta \rho_{C_{60}}$ in Equation 3 remains at its thermal equilibrium value and the absorption coefficient is approximately independent of intensity.

Interactions are difficult to study in thermal equilibrium since the steady-state populations are determined by detailed balance rather than by the particular nature of the interactions. To probe collision cross sections, we optically pump the 8.4- μ m vibrational band of $^{12}C_{60}$ to prepare an excited steady-state rovibrational population distribution (**Figure 8***b*). The optical pumping of $^{12}C_{60}$ is facilitated by the three orders of magnitude enhancement of optical power inside the high-finesse ($\mathcal{F}=12,500$) cavity and high spectral power density of the QCL. When the Rabi frequency becomes comparable to relaxation and dephasing rates, $\Delta \rho_{C_{60}}$ is reduced from its thermal equilibrium value and absorption saturates (125). Therefore, the saturation intensity provides a measure of total dephasing and relaxation rates.

Saturated ¹²C₆₀ absorption spectra were taken for several different buffer gas species. Depending on the optical pumping frequency, either individual or multiple states can be pumped at a time,

allowing the rotation and vibration inelastic collision rates to be disentangled (**Figure 8***c,d*). To extract quantitative collision cross sections, a rate equation model that simultaneously accounts for the inelastic collisions and diffusion of molecules through the optical pumping region is fit to the measured absorption spectra (**Figure 9***a,b*). For each buffer gas species, a complete dataset consisted of Q- and R-branch spectra acquired over several optical pumping rates, buffer gas densities, and J's in order to eliminate fitting correlations. The model assumed an exponential gap law for state-to-state rotational relaxation (not directly resolvable in the experiment) and ab initio elastic cross sections for C_{60} -buffer gas collisions. The vibrational relaxation is modeled as the two-step process depicted in **Figure 8***b*: a J-independent cross section σ_{vib} for quenching the initially prepared excited vibrational state n' = 1 into a dense bath of dark vibrational states, followed by another J-independent cross section σ'_{vib} for returning to the ground state n'' = 0. Here, n refers to the vibrational quantum number. The fitting parameters include σ_{vib} , σ'_{vib} , and $\langle \sigma_{rot} \rangle$ for each

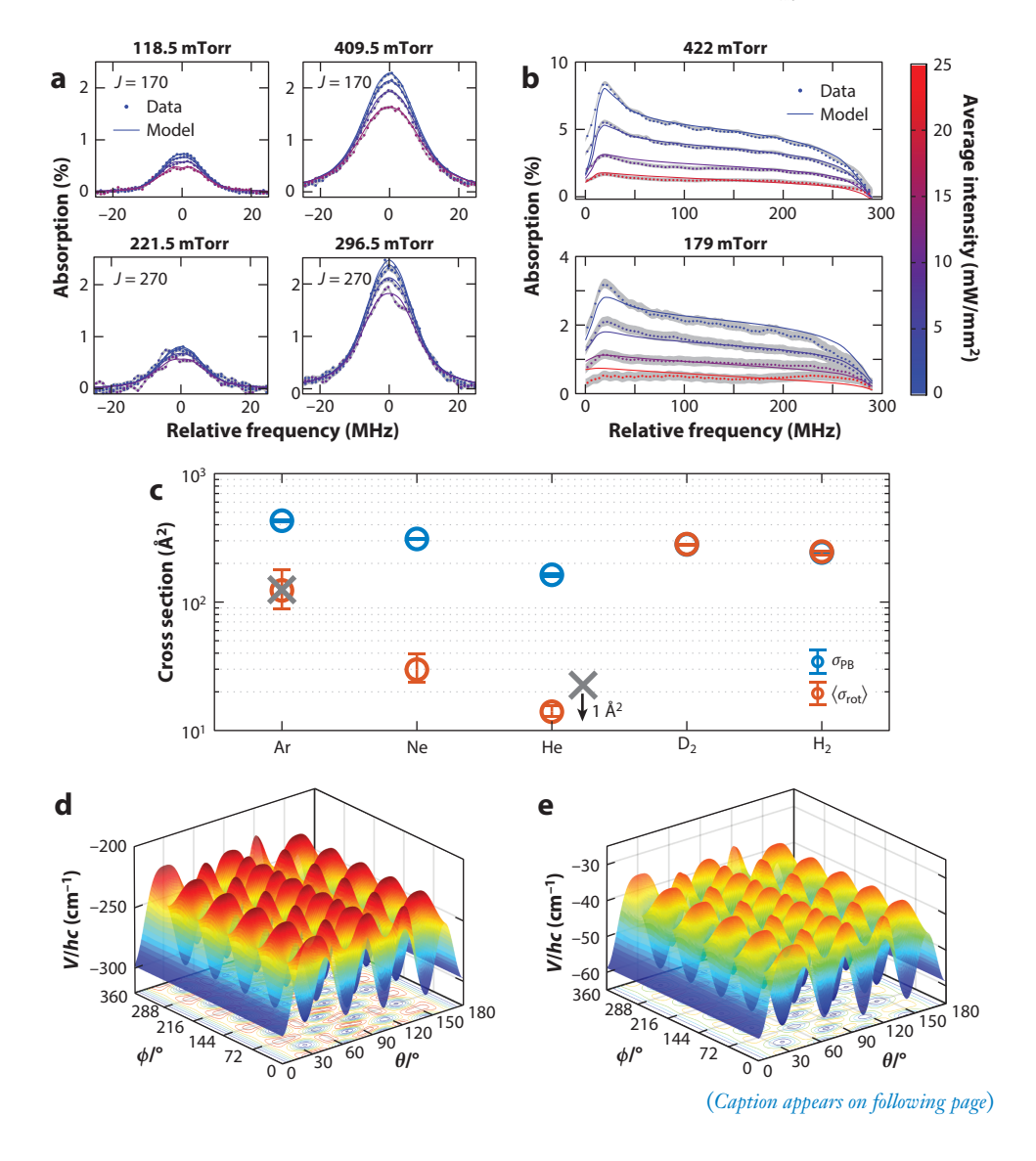


Figure 9 (Figure appears on preceding page)

Extracting ¹²C₆₀ – buffer gas collision cross sections and interaction potentials. (a) Rate equation model fits to $^{12}C_{60}$ -Ar R-branch saturated absorption data. Also shown are typical R-branch absorption data at J=170 (top) and J = 270 (bottom) and corresponding rate equation fits. Good agreement is obtained by modeling state-to-state rotational relaxation with an exponential gap law. Gray bands indicate the 1σ uncertainty in the data. (b) Rate equation model fits to ¹²C₆₀-Ar Q-branch saturated absorption data. The Q-branch absorption data and rate equation model fit correspond to high (upper panel) and low (lower panel) Ar pressure (specified above each panel) at four pumping intensities. Only every fourth data point is plotted for clarity. Gray bands indicate standard uncertainty in the data dominated by residual etalons in the optical setup. The color of traces in panels a and b corresponds to different pumping intensities, indicated by the color bar. (c) Average rotational inelastic collision cross sections $\langle \sigma_{\rm rot} \rangle$ extracted from the rate equation model fits to $^{12}\text{C}_{60}$ -buffer gas saturated absorption data. The total pressure-broadening cross sections σ_{PB} , obtained from R-branch fits, are plotted for reference. Error bars indicate 68% confidence intervals and include the uncertainty on the effective diffusion length of the molecules out of the cavity mode. Calculated values of $\langle \sigma_{\rm rot} \rangle$ for $^{12}{\rm C}_{60}$ –Ar and $^{12}{\rm C}_{60}$ –He are plotted as gray crosses for comparison. (d) Potential energy surfaces for $^{12}C_{60}$ –Ar interactions, calculated at the equilibrium bond length of 7.2 Å. Polar θ and azimuthal ϕ angles are defined with respect to a Cartesian coordinate system with its x and z axes along two- and fivefold symmetry axes of ¹²C₆₀, respectively. (e) Potential energy surface for ¹²C₆₀–He calculated at the equilibrium bond length of 7.0 Å. Note the change in vertical scale. The potential anisotropy for this complex is significantly reduced compared to that of ¹²C₆₀-Ar. Figure adapted with permission from Reference 72.

buffer gas species, where $\langle \rangle$ denotes thermal averaging over initial and final rotational states. Diffusion of new molecules into the interaction region is found to dominate over $\sigma'_{\rm vib}$, whose best-fit value is indistinguishable from zero. This is not surprising due to the considerable energy gap (270 cm⁻¹) between the ground state and the first excited vibrational state (69).

6.3. C₆₀ Collision Cross Sections and the Interaction Potential

The fitted inelastic cross sections revealed interesting trends of the collision cross sections between $^{12}C_{60}$ and the buffer gas (**Figure 9c**): $\langle \sigma_{\rm rot} \rangle$ decreases by a factor of ten from $^{12}C_{60}$ –Ar $(123^{+60}_{-36}\text{Å}^2)$ to $^{12}C_{60}$ –He (14^{+2}_{-1}Å^2) . Despite being of a similar mass as He, the molecules D_2 $(282^{+6}_{-10}\text{Å}^2)$ and H_2 $(247^{+9}_{-21}\text{Å}^2)$ feature significantly larger $\langle \sigma_{\rm rot} \rangle$, even saturating the upper bound set by the total pressure broadening cross section σ_{PB} . $\sigma_{\rm vib}$ was unmeasurable $(<10^{-2}\text{Å}^2)$ for all systems except $^{12}C_{60}$ –Ar $(0.07\pm0.03\text{Å}^2)$.

These results can be understood as follows: For the monatomic buffer gases, rotational energy exchange arises from the anisotropic polarizability, which is lowest for $^{12}C_{60}$ –He due to the low polarizability of He. H_2 and D_2 , on the other hand, can effect rotational relaxation from long range due to their quadrupole moments, leading to the increased $\langle\sigma_{rot}\rangle$. Since $\langle\sigma_{rot}\rangle\sim\sigma_{PB}$, it can also be inferred that these long-range rotational quenching interactions dominate over the pure dephasing (elastic) collisions. An important number is the ratio σ_{el} : $\sigma_{vib}\approx 3\times 10^4$ for the $^{12}C_{60}$ –Ar system. This is about four orders of magnitude smaller than in previous cold molecule studies (75), indicating an unusually large vibrational quenching cross section; however, one should keep in mind that the vibrational density of states of $^{12}C_{60}$ at 8.4 μm is four to five orders of magnitude higher than that of the usual diatomic molecules considered.

The best-fit rotational state-to-state cross sections in the exponential gap law model for the $^{12}\mathrm{C}_{60}$ -He system $\sigma_{\mathrm{rot}}(J_i \to J_f) \lesssim 0.1 \, \mathring{\mathrm{A}}^2$ are two to three orders of magnitude lower than those for rotational quenching of H₂CO-He (126) or H₂S-He (127). While the experimental conditions in these studies, specifically J and temperature, are much lower than in the $^{12}\mathrm{C}_{60}$ work, this comparison provides the first indication that rotations of $^{12}\mathrm{C}_{60}$ may be unusually well-protected during collisions with noble gases in spite of its low rotational constant. Direct state-to-state

measurements of rotational quenching collision cross sections at lower temperature will help shore up this comparison.

Figure 9d,e plots the calculated interaction potentials for $^{12}C_{60}$ –Ar and $^{12}C_{60}$ –He at their equilibrium bond lengths. Based on accurate calculations of the various anisotropic terms in the potential energy surfaces, $\langle \sigma_{\rm rot} \rangle$ was predicted to be 126 Ų for $^{12}C_{60}$ –Ar and 1 Ų for $^{12}C_{60}$ –He (72, 128). The significantly reduced potential anisotropy of the $^{12}C_{60}$ –He complex is reflected in the small value of $\langle \sigma_{\rm rot} \rangle$. These are plotted alongside the experimental data in **Figure 9c** for comparison. Excellent agreement is obtained for $^{12}C_{60}$ –Ar, while $^{12}C_{60}$ –He features a significant discrepancy. In the latter case, the predicted $\langle \sigma_{\rm rot} \rangle$ value arises from the linear combination of many small terms of opposite signs in the anisotropic potential, which may lead to a large uncertainty. This suggests that saturated absorption spectra of $^{12}C_{60}$ can benchmark ab initio calculations of this unique collision complex.

7. CONCLUSION AND OUTLOOK

In spite of decades of progress in $^{12}C_{60}$ research since its initial observation in 1985, the observation of rotationally resolved infrared spectra of the 8.4 μ m band in $^{12}C_{60}$ in 2019 and continued experimental advances since then have led to a series of high-resolution spectroscopic measurements that have provided the clearest understanding of the structure, dynamics, and interactions of individual gas phase $^{12}C_{60}$ molecules to date. Through these recent activities a number of firsts in high-resolution molecular spectroscopy have been achieved: rotational state resolution in infrared spectra for the largest and most symmetric molecule to date (60); observation of the complete disappearance of rotational lines due to icosahedral symmetry (80); the observation and assignment of icosahedral tensor splittings (42); and quantitative measurements of unusually small and unusually large rotational and vibrational quenching collision cross sections of $^{12}C_{60}$, respectively (72).

We hope this work emphasizes that large molecules are important and complementary platforms for uncovering novel emergent behavior not present in other composite quantum systems, made possible by their free rotations, rotation-vibration coupling, and perfect rotational symmetry (42), or as probes of their local environment by analyzing absorption profiles in high-resolution and high-sensitivity spectra (72).

Finally, we note the many further scientific opportunities available with $^{12}C_{60}$ alone (e.g., in other vibrational bands not yet measured) or with its many derivative compounds such as higher fullerenes. The rare $^{13}C_{60}$ (129) might be exploited for its enormous Hilbert space for quantum information processing in a spatially compact platform. We believe the lessons learned from this model molecule may be ported over to the understanding and eventually quantum control of other complex molecular systems.

DISCLOSURE STATEMENT

The authors are not aware of any affiliations, memberships, funding, or financial holdings that might be perceived as affecting the objectivity of this review.

ACKNOWLEDGMENTS

We gratefully acknowledge the significant contributions of many current and former laboratory members over the past few years to quantum state–resolved investigations of $^{12}C_{60}$, including Y.-C. Chan, P.B. Changala, Q. Liang, D. Rosenberg, A. Scheck, J. Toscano, and M.L. Weichman. We also gratefully acknowledge many collaborators, including P.J.D. Crowley, M.E. Fermann, J. Kłos, S. Kotochigova, K.F. Lee, D.J. Nesbitt, T.V. Tscherbul, and N.Y. Yao. Funding support over the years has been provided by an Air Force Office of Scientific Research grant

(FA9550-19-1-0148), a National Science Foundation Quantum Leap Challenge Institutes grant (QLCI OMA-2016244), a National Science Foundation grant (Phys-1734006), and the National Institute of Standards and Technology.

LITERATURE CITED

- Georgakilas V, Perman JA, Tucek J, Zboril R. 2015. Broad family of carbon nanoallotropes: classification, chemistry, and applications of fullerenes, carbon dots, nanotubes, graphene, nanodiamonds, and combined superstructures. Chem. Rev. 115(11):4744

 –822
- Adler F, Masłowski P, Foltynowicz A, Cossel KC, Briles TC, et al. 2010. Mid-infrared Fourier transform spectroscopy with a broadband frequency comb. Opt. Express 18(21):21861–72
- 3. Fu B, Zhang C, Lyu W, Sun J, Shang C, et al. 2020. Recent progress on laser absorption spectroscopy for determination of gaseous chemical species. *Appl. Spectrosc. Rev.* 57(2):112–52
- Moore DS. 2004. Instrumentation for trace detection of high explosives. Rev. Sci. Instrum. 75(8):2499–512
- McCurdy MR, Bakhirkin Y, Wysocki G, Lewicki R, Tittel FK. 2007. Recent advances of laserspectroscopy-based techniques for applications in breath analysis. 7. Breath Res. 1(1):014001
- Liang Q, Chan YC, Changala PB, Nesbitt DJ, Ye J, Toscano J. 2021. Ultrasensitive multispecies spectroscopic breath analysis for real-time health monitoring and diagnostics. PNAS 118(40):e2105063118
- Liang Q, Chan YC, Toscano J, Bjorkman KK, Leinwand LA, et al. 2023. Breath analysis by ultra-sensitive broadband laser spectroscopy detects SARS-CoV-2 infection. J. Breath Res. 17(3):036001
- Brown SS. 2003. Absorption spectroscopy in high-finesse cavities for atmospheric studies. Chem. Rev. 103(12):5219–38
- Li J, Yu Z, Du Z, Ji Y, Liu C. 2020. Standoff chemical detection using laser absorption spectroscopy: a review. Remote Sens. 12(17):2771
- Funke HH, Grissom BL, McGrew CE, Raynor MW. 2003. Techniques for the measurement of trace moisture in high-purity electronic specialty gases. Rev. Sci. Instrum. 74(9):3909–33
- 11. Merrill KM, Ridgway ST. 1979. Infrared spectroscopy of stars. Annu. Rev. Astron. Astrophys. 17:9-41
- 12. Herbig GH. 1995. The diffuse interstellar bands. Annu. Rev. Astron. Astrophys. 33:19-73
- 13. Snow TP. 2001. The unidentified diffuse interstellar bands as evidence for large organic molecules in the interstellar medium. Spectrochim. Acta Part A Mol. Biomol. Spectrosc. 57(4):615–26
- Campbell EK, Holz M, Gerlich D, Maier JP. 2015. Laboratory confirmation of C₆₀⁺ as the carrier of two diffuse interstellar bands. Nature 523(7560):322–23
- Encrenaz T. 2022. Invited review: infrared spectroscopy of planetary atmospheres: searching for insights into their past and present histories. *Icarus* 376:114885
- Patra S, Germann M, Karr JP, Haidar M, Hilico L, et al. 2020. Proton-electron mass ratio from laser spectroscopy of HD⁺ at the part-per-trillion level. Science 369(6508):1238–41
- Modugno G, Inguscio M, Tino GM. 1998. Search for small violations of the symmetrization postulate for spin-0 particles. Phys. Rev. Lett. 81(22):4790–93
- Mazzotti D, Cancio P, Giusfredi G, Inguscio M, Natale PD. 2001. Search for exchange-antisymmetric states for spin-0 particles at the 10⁻¹¹ level. Phys. Rev. Lett. 86(10):1919–22
- Pastor PC, Galli I, Giusfredi G, Mazzotti D, Natale PD. 2015. Testing the validity of Bose-Einstein statistics in molecules. Phys. Rev. A 92:063820
- Hall JL, Hollberg L, Long-sheng M, Baer T, Robinson HG. 1981. Progress toward phase-stable optical frequency standards. J. Phys. Colloque 42(12):C8-59-71
- Ye J, Ma LS, Hall JL. 1998. Ultrasensitive detections in atomic and molecular physics: demonstration in molecular overtone spectroscopy. 7. Opt. Soc. Am. B 15(1):6–15
- 22. Wilson E, Decius J, Cross P. 1980. Molecular Vibrations: The Theory of Infrared and Raman Vibrational Spectra. New York: Dover
- 23. Herzberg G. 1945. Molecular Spectra and Molecular Structure II: Infrared and Raman of Polyatomic Molecules. Toronto: D. Van Nostrand Co.
- 24. Townes CH, Schawlow A. 1975. Microwave Spectroscopy. New York: Dover

- Weeks DE. 1992. Isotopic and anharmonic perturbations to the dipole active vibrational modes of buckminsterfullerene. 7. Chem. Phys. 96(10):7380–93
- Harter WG, Patterson CW. 1984. Rotational energy surfaces and high-\(\textit{7} \) eigenvalue structure of polyatomic molecules. \(\textit{7} \). Chem. Phys. 80(9):4241–61
- Galatry L. 1961. Simultaneous effect of Doppler and foreign gas broadening on spectral lines. Phys. Rev. 122(4):1218–23
- Rautian SG, Sobel'man II. 1967. The effect of collisions on the Doppler broadening of spectral lines. Sov. Phys. Usp. 9(5):701–16
- Weber EW, Jungmann K. 1980. Influence of elastic and inelastic collisions on density shift and broadening. Phys. Lett. 81(January):223–27
- Fröchtenicht R, Toennies JP, Vilesov A. 1994. High-resolution infrared spectroscopy of SF₆ embedded in He clusters. Chem. Phys. Lett. 229(1–2):1–7
- Hartmann M, Miller RE, Toennies JP, Vilesov AF. 1996. High-resolution molecular spectroscopy of van der Waals clusters in liquid helium droplets. Science 272:1631–34
- Close JD, Federmann F, Hoffmann K, Quaas N. 1997. Absorption spectroscopy of C₆₀ molecules isolated in helium droplets. Chem. Phys. Lett. 276:393–98
- Verma D, Tanyag RMP, O'Connell SM, Vilesov AF. 2019. Infrared spectroscopy in superfluid helium droplets. Adv. Phys. X 4(1):1553569
- Uehara K, Shimizu T, Shimoda K. 1968. High-resolution stark spectroscopy of molecules by infrared and far-infrared masers. IEEE 7. Quantum Electron. 4(11):728–32
- Koloshnikov VG, Kuritsyn YA, Pak I, Ulitskiy NI, Kharlamov BM, et al. 1980. Zeeman effect in the IR spectrum of a molecule without EN electronic moment. Observation with a tunable diode laser. Opt. Commun. 35(2):213–17
- Chattopadhyay A, Boxer SG. 1995. Vibrational stark effect spectroscopy. J. Am. Chem. Soc. 117(4):1449– 50
- Fried SD, Boxer SG. 2015. Measuring electric fields and noncovalent interactions using the vibrational stark effect. Acc. Chem. Res. 48(4):998–1006
- Changala PB, Weichman ML, Lee KF, Fermann ME, Ye J. 2019. Rovibrational quantum state resolution of the C₆₀ fullerene. Science 363(6422):49–54
- 39. Litvin DB. 1991. The icosahedral point groups. Acta Crystallograph. Sect. A 47(2):70-73
- Bunker PR, Jensen P. 1999. Spherical top molecules and the molecular symmetry group. Mol. Phys. 97:255–64
- 41. Atkins PW, Child MS, Phillips CSG. 2006. Tables for Group Theory, vol. 6. Oxford: Oxford Univ. Press
- 42. Liu LR, Rosenberg D, Changala PB, Crowley PJ, Nesbitt DJ, et al. 2023. Ergodicity breaking in rapidly rotating C₆₀ fullerenes. *Science* 381(6659):778–83
- Kroto HW, Heath JR, O'Brien S, Curl R, Smalley R. 1985. C₆₀: buckminsterfullerene. Nature 318:162–63
- 44. Osawa E. 1970. Superaromaticity. Kagaku 25:854-63
- 45. Schmalz TG, Seitz WA, Klein DJ, Hite GE. 1986. C60 carbon cages. Chem. Phys. Lett. 130(3):203-7
- 46. Kroto H. 1988. Space, stars, C₆₀, and soot. Science 242:1139-45
- 47. Kroto HW. 1987. The stability of the fullerenes C_n , with $n=24,\,28,\,32,\,36,\,50,\,60$ and 70. Nature 329(8):529-31
- Haufler RE, Chai Y, Chibante LPF, Conceicao J, Jin C, et al. 1990. Carbon arc generation of C₆₀. MRS Online Proc. Libr. 206:627–37
- Krätschmer W, Lamb LD, Fostiropoulos K, Huffman DR. 1990. Solid C₆₀: a new form of carbon. *Nature* 347:354–58
- Krätschmer W, Fostiropoulos K, Huffman DR. 1990. The infrared and ultraviolet absorption spectra
 of laboratory-produced carbon dust: evidence for the presence of the C₆₀ molecule. *Chem. Phys. Lett.*170(2–3):167–70
- Bethune DS, Meijer G, Tang WC, Rosen HJ, Golden WG, et al. 1991. Vibrational Raman and infrared spectra of chromatographically separated C₆₀ and C₇₀ fullerene clusters. *Chem. Phys. Lett.* 179(1–2):181– 86

- Stanton RE, Newton MD. 1988. Normal vibrational modes of buckminsterfullerene. J. Phys. Chem. 92(8):2141–45
- Weeks DE, Harter WG. 1989. Rotation-vibration spectra of icosahedral molecules. II. Icosahedral symmetry, vibrational eigenfrequencies, and normal modes of buckminsterfullerene. J. Chem. Phys. 90(9):4744–71
- 54. Califano S. 1976. Vibrational States. Hoboken, NJ: Wiley
- Nesbitt DJ, Field RW. 1996. Vibrational energy flow in highly excited molecules: role of intramolecular vibrational redistribution. 7. Phys. Chem. 100(31):12735–56
- Whitten GZ, Rabinovitch BS. 1963. Accurate and facile approximation for vibrational energy-level sums.
 Chem. Phys. 38(10):2466–73
- Stewart GM, McDonald JD. 1983. Intramolecular vibrational relaxation from C–H stretch fundamentals. J. Chem. Phys. 78(6):3907–15
- Buckingham GT, Chang CH, Nesbitt DJ. 2013. High-resolution rovibrational spectroscopy of jetcooled phenyl radical: the v₁9 out-of-phase symmetric CH stretch. 7. Phys. Chem. A 117(39):10047–57
- Spaun B, Changala PB, Patterson D, Bjork BJ, Heckl OH, et al. 2016. Continuous probing of cold complex molecules with infrared frequency comb spectroscopy. *Nature* 533(7604):517–20
- Changala PB, Spaun B, Patterson D, Doyle JM, Ye J. 2016. Sensitivity and resolution in frequency comb spectroscopy of buffer gas cooled polyatomic molecules. Appl. Phys. B Lasers Opt. 122(12):292
- Lederman SM, Runnels JH, Marcus RA. 1983. Densities of vibrational states of given symmetry species and their use in statistical estimates involving coriolls and anharmonic effects. J. Phys. Chem. 87(22):4364– 67
- Pechukas P. 1984. Comment on 'densities of vibrational states of given symmetry species.' J. Phys. Chem. 88:828
- Peng LW, Keelan BW, Semmes DH, Zewail AH. 1988. Dynamics of intramolecular vibrational energy redistribution in deuteriated anthracenes: rotational band contour analysis and time-resolved measurements. *7. Phys. Chem.* 92(19):5540–49
- 64. Bigwood R, Gruebele M, Leitner DM, Wolynes PG. 1998. The vibrational energy flow transition in organic molecules: theory meets experiment. *PNAS* 95(11):5960–64
- 65. Hippler M, Pfab R, Quack M. 2003. Isotopomer-selective overtone spectroscopy of jet-cooled benzene by ionization detected IR + UV double resonance: The N=2 CH chromophore absorption of $^{12}C_6H_6$ and near 6000 cm $^{13}C^{12}C_5H_6$. 7. Phys. Chem. A 107(49):10743–52
- Benten RSV, Liu Y, Abel B. 2010. Dynamical consequences of symmetry breaking in benzene and difluorobenzene. J. Chem. Phys. 133(13):134306
- Tuttle WD, Gardner AM, Whalley LE, Kemp DJ, Wright TG. 2019. Effects of symmetry, methyl groups and serendipity on intramolecular vibrational energy dispersal. *Phys. Chem. Chem. Phys.* 21(26):14133–52
- Ramachandran G, Manogaran S. 2006. Vibrational spectra of adamantanes X₁₀H₁₆ and diamantanes X₁₄H₂₀ (X=C, Si, Ge, Sn): a theoretical study. 7. Mol. Struct. THEOCHEM 766(2–3):125–35
- 69. Menendez J, Page JB. 1995. Vibrational spectroscopy of C₆₀. J. Mol. Spectrosc. 173(2):431-41
- Oldani M, Andrist M, Bauder A, Robiette AG. 1985. Pure rotational spectra of methane and methane-d₄
 in the vibrational ground state observed by microwave Fourier transform spectroscopy. *J. Mol. Spectrosc.*110(1):93–105
- Iglesias-Groth S, Cataldo F, Manchado A. 2011. Infrared spectroscopy and integrated molar absorptivity of C₆₀ and C₇₀ fullerenes at extreme temperatures. MNRAS 413(1):213–22
- Liu LR, Changala PB, Weichman ML, Liang Q, Toscano J, et al. 2022. Collision-induced C₆₀ rovibrational relaxation probed by state-resolved nonlinear spectroscopy. PRX Quantum 3(3):030332
- Forrey RC, Kharchenko V, Balakrishnan N, Dalgarne A. 1999. Vibrational relaxation of trapped molecules. Phys. Rev. A 59(3):2146–52
- Pauly H. 2000. Atom, Molecule, and Cluster Beams I: Basic Theory, Production and Detection of Thermal Energy Beams. Berlin: Springer
- Campbell WC, Doyle JM. 2009. Cooling, trap loading, and beam production using a cryogenic helium buffer gas. In *Cold Molecules: Theory, Experiment, Applications*, ed. R Krems, B Friedrich, WC Stwalley, pp. 473–508. Boca Raton, FL: CRC Press

- Brumfield BE, Stewart JT, McCall BJ. 2012. Extending the limits of rotationally resolved absorption spectroscopy: pyrene. 7. Phys. Chem. Lett. 3(15):1985–88
- Doyle JM, Friedrich B, Kim J, Patterson D. 1995. Buffer-gas loading of atoms and molecules into a magnetic trap. Phys. Rev. A 52(4):R2515–18
- Hillenkamp M, Keinan S, Even U. 2003. Condensation limited cooling in supersonic expansions. J. Chem. Phys. 118(19):8699–705
- Wallraff P, Yamada KM, Winnewisser G. 1987. Determination of the vibrational temperature of OCS in a supersonic free jet. J. Mol. Spectrosc. 126(1):78–81
- Chan YC, Liu LR, Scheck A, Nesbitt DJ, Ye J, Rosenberg D. 2024. Observation of full contrast icosahedral Bose-Einstein statistics in laser desorbed, buffer gas cooled C₆₀. arXiv:2406.13907 [physics.atom-ph]
- 81. Adler F, Thorpe MJ, Cossel KC, Ye J. 2010. Cavity-enhanced direct frequency comb spectroscopy: technology and applications. *Annu. Rev. Anal. Chem.* 3:175–205
- Shumakova V, Heckl OH. 2024. A short guide to recent developments in laser-based gas phase spectroscopy, applications, and tools. APL Photon. 9(1):010803
- 83. Maslowski P, Lee KF, Johansson AC, Khodabakhsh A, Kowzan G, et al. 2016. Surpassing the pathlimited resolution of Fourier-transform spectrometry with frequency combs. *Phys. Rev. A* 93(2):021802
- Faist J, Capasso F, Sivco DL, Sirtori C, Hutchinson AL, Cho AY. 1994. Quantum cascade laser. Science 264(5158):553–56
- 85. Dahmani B, Hollberg L, Drullinger R. 1987. Frequency stabilization of semiconductor lasers by resonant optical feedback. Opt. Lett. 12(11):876–78
- Laurent P, Clairon A, Breant C. 1989. Frequency noise analysis of optically self-locked diode lasers. IEEE 7. Quantum Electron. 25(6):1131–42
- 87. Ohshima S-I, Schnatz H. 1991. Optimization of injection current and feedback phase of an optically self-locked laser diode. *7. Appl. Phys.* 71:3114–17
- Maisons G, Carbajo PG, Carras M, Romanini D. 2010. Optical-feedback cavity-enhanced absorption spectroscopy with a quantum cascade laser. Opt. Lett. 35(21):3607–9
- Burkart J, Romanini D, Kassi S. 2013. Optical feedback stabilized laser tuned by single-sideband modulation. Opt. Lett. 38(12):2062–64
- Zhao G, Tian J, Hodges JT, Fleisher AJ. 2021. Frequency stabilization of a quantum cascade laser by weak resonant feedback from a Fabry–Perot cavity. Opt. Lett. 46(13):3057–60
- di Lauro C. 2020. Spectra of spherical top molecules. In Rotational Structure in Molecular Infrared Spectra, pp. 223–41. Amsterdam: Elsevier
- Weeks DE, Harter WG. 1991. Rotation-vibration scalar coupling chi coefficients and spectroscopic band shapes of buckminsterfullerene. Chem. Phys. Lett. 176(2):209–16
- Hedberg K, Hedberg L, Bethune DS, Brown CA, Dorn HC, et al. 1991. Bond lengths in free molecules of buckminsterfullerene, C⁶⁰, from gas-phase electron diffraction. Science 254(5030):410–12
- 94. Pirali O, Boudon V, Oomens J, Vervloet M. 2012. Rotationally resolved infrared spectroscopy of adamantane. J. Chem. Phys. 136(2):024310
- Yannouleas C, Landman U. 2007. Symmetry breaking and quantum correlations in finite systems: studies
 of quantum dots and ultracold Bose gases and related nuclear and chemical methods. Rep. Prog. Phys.
 70(12):2067–148
- Birman JL, Nazmitdinov RG, Yukalov VI. 2013. Effects of symmetry breaking in finite quantum systems. Phys. Rep. 526(1):1–91
- Hecht KT. 1961. The vibration-rotation energies of tetrahedral XY₄ molecules. J. Mol. Spectrosc. 5(1–6):355–89
- 98. Raynal J. 1984. Determination of point group harmonics for arbitrary *j* by a projection method. II. Icosahedral group, quantization along an axis of order 5. *J. Math. Phys.* 25(12):3375–81
- 99. Harter WG, Weeks DE. 1989. Rotation-vibration spectra of icosahedral molecules. I. Icosahedral symmetry analysis and fine structure. 7. Chem. Phys. 90(9):4727–43
- 100. Wigner EP. 1967. Random matrices in physics. SIAM Rev. 9(1):1009001
- Berry MV, Tabor M. 1977. Level clustering in the regular spectrum. Proc. R. Soc. Lond. A Math. Phys. Sci. 356(1686):375–94

- 102. Berry MV. 1987. The Bakerian lecture, 1987 quantum chaology. Proc. R. Soc. A 413:183-98
- Oganesyan V, Huse DA. 2007. Localization of interacting fermions at high temperature. Phys. Rev. B 75(15):155111
- Atas YY, Bogomolny E, Giraud O, Roux G. 2013. Distribution of the ratio of consecutive level spacings in random matrix ensembles. *Phys. Rev. Lett.* 110(8):084101
- Sundberg RL, Abramson E, Kinsey JL, Field RW. 1985. Evidence of quantum ergodicity in stimulated emission pumping spectra of acetylene. 7. Chem. Phys. 83(2):466–75
- Zimmermann T, Koppel H, Cederbaum LS, Persch G, Demtroder W. 1988. Confirmation of randommatrix fluctuations in molecular spectra. Phys. Rev. Lett. 61(1):3–6
- Harter WG. 1981. Theory of hyperfine and superfine levels in symmetric polyatomic molecules. II.
 Elementary cases in octahedral hexafluoride molecules. Phys. Rev. A 24(1):192–263
- Harter WG. 1984. Patterns of energy levels and spectra for polyatomic molecules. J. Stat. Phys. 36(5–6):749–77
- 109. Harter WG. 1988. Computer graphical and semiclassical approaches to molecular rotations and vibrations. *Comput. Phys. Rep.* 8(6):319–94
- Sadovskii DA, Zhilinskii BI, Champion JP, Pierre G. 1990. Manifestation of bifurcations and diabolic points in molecular energy spectra. 7. Chem. Phys. 92(3):1523–37
- Cohan NV. 1958. The spherical harmonics with the symmetry of the icosahedral group. Math. Proc. Camb. Philos. Soc. 54(1):28–38
- 112. Zheng Y, Doerschuk PC. 1996. Explicit orthonormal fixed bases for spaces of functions that are totally symmetric under the rotational symmetries of a platonic solid. *Acta Crystallogr.* 52:221–35
- 113. Cornwell JF. 1997. Group Theory in Physics. Cambridge, MA: Academic Press
- 114. Landau L, Lifshitz E. 1976. Mechanics, Vol. 1. Oxford, UK: Butterworth-Heinemann. 3rd ed.
- 115. Dorney AJ, Watson JKG. 1972. Forbidden rotational spectra of polyatomic molecules: Stark effects and $\Delta J = 0$ transitions of T_d molecules. J. Mol. Spectrosc. 42:135–48
- Landau L, Lifshitz E. 1958. Quantum Mechanics: Non-Relativistic Theory, Vol. 3. New York: Pergamon Press
- Fischer S, Laubereau A. 1975. Dephasing processes of molecular vibrations in liquids. Chem. Phys. Lett. 35(1):6–12
- 118. Diestler DJ, Manz J. 1977. Model for vibrational dephasing of diatomic molecules in liquids liquid N_2 and O_2 . Mol. Phys. 33(1):227–44
- Wertheimer RK. 1978. On the theory of spectral line broadening: vibrational dephasing and resonance energy transfer in molecular liquids. Mol. Phys. 35(1):257–82
- Hindmarsh WR, Farr JM. 1973. Collision broadening of spectral lines by neutral atoms. Prog. Quantum Elect. 2:143–214
- Vutha AC, Kirchner T, Dubé P. 2017. Collisional frequency shift of a trapped-ion optical clock. Phys. Rev. A 96(2):022704
- 122. Gordon RG. 1966. Theory of the width and shift of molecular spectral lines in gases. *J. Chem. Phys.* 44(8):3083–89
- Demtröder W. 2005. Molecular Physics: Theoretical Principles and Experimental Methods. Weinheim: Wiley-VCH
- 124. Weisskopf V. 1933. The intensity and structure of spectral lines. Observatory 56:291-308
- 125. Demtröder W. 2008. Laser Spectroscopy, Vol. 2: Experimental Techniques. Berlin: Springer
- 126. Mengel M, Lucia FCD. 2000. Helium and hydrogen induced rotational relaxation of H₂CO observed at temperatures of the interstellar medium. *Astrophys.* 7, 543:271
- Ball CD, Lucia FCD. 1998. Direct measurement of rotationally inelastic cross sections at astrophysical and quantum collisional temperatures. Phys. Rev. Lett. 81:305–8
- Kłos J, Tiesinga E, Kotochigova S. 2024. Quantum scattering of icosahedron fullerene C₆₀ with noblegas atoms. Sci. Rep. 14(1):9267
- 129. Chun Chen C, Lieber CM. 1992. Synthesis of pure ¹³C₆₀ and determination of the isotope effect for fullerene superconductors. *J. Am. Chem. Soc.* 114(8):3141–42